A&A, 683, A166 (2024)
https://doi.org/10.1051/0004-6361/202346999

Astronomy & Astrophysics

TOI-4860 b, a short-period giant planet transiting an M3.5 dwarf

J. M. Almenara[1,2], X. Bonfils[1], E. M. Bryant[3,4], A. Jordán[5,6,7], G. Hébrard[8,9], E. Martioli[10,8], A. C. M. Correia[11,12], N. Astudillo-Defru[13], C. Cadieux[14], L. Arnold[15], É. Artigau[14], G. Á. Bakos[16], S.C.C. Barros[17,18], D. Bayliss[4], F. Bouchy[2], G. Boué[12], R. Brahm[5,6,7], A. Carmona[1], D. Charbonneau[19], D. R. Ciardi[20], R. Cloutier[21], M. Cointepas[1,2], N. J. Cook[14], N. B. Cowan[22,23], X. Delfosse[1], J. Dias do Nascimento[19,24], J.-F. Donati[25], R. Doyon[14], T. Forveille[1], P. Fouqué[25], E. Gaidos[26], E. A. Gilbert[27], J. Gomes da Silva[17], J. D. Hartman[16], K. Hesse[28], M. J. Hobson[29,6], J. M. Jenkins[30], F. Kiefer[31], V. B. Kostov[32,33], J. Laskar[12], M. Lendl[2], A. L'Heureux[14], J. H. C. Martins[17], K. Menou[34,35,36], C. Moutou[25], F. Murgas[37,38], A. S. Polanski[39,20], D. Rapetti[30,40], E. Sedaghati[41], and H. Shang[42]

(Affiliations can be found after the references)

Received 25 May 2023 / Accepted 8 January 2024

ABSTRACT

We report the discovery and characterisation of a giant transiting planet orbiting a nearby M3.5V dwarf (d = 80.4 pc, G = 15.1 mag, K=11.2 mag, $R_\star$ = 0.358 ± 0.015 $R_\odot$, $M_\star$ = 0.340 ± 0.009 $M_\odot$). Using the photometric time series from TESS sectors 10, 36, 46, and 63 and near-infrared spectrophotometry from ExTrA, we measured a planetary radius of 0.77 ± 0.03 R_J and an orbital period of 1.52 days. With high-resolution spectroscopy taken by the CFHT/SPIRou and ESO/ESPRESSO spectrographs, we refined the host star parameters ([Fe/H] = 0.27 ± 0.12) and measured the mass of the planet (0.273 ± 0.006 M_J). Based on these measurements, TOI-4860 b joins the small set of massive planets (>80 M_E) found around mid to late M dwarfs (<0.4 $R_\odot$), providing both an interesting challenge to planet formation theory and a favourable target for further atmospheric studies with transmission spectroscopy. We identified an additional signal in the radial velocity data that we attribute to an eccentric planet candidate (e = 0.66 ± 0.09) with an orbital period of 427 ± 7 days and a minimum mass of 1.66 ± 0.26 M_J, but additional data would be needed to confirm this.

Key words. techniques: photometric – techniques: radial velocities – stars: individual: TOI-4860 – stars: low-mass – planetary systems

1. Introduction

Twenty-five years ago, the discovery of GJ 876 b, a planet with twice the mass of Jupiter, marked an important milestone in exoplanet research (Marcy et al. 1998; Delfosse et al. 1998). It was the first planet detected around an M dwarf, and only the ninth exoplanet found around a main-sequence star at that time. The discovery of GJ 876 b soon after the detection of 51 Pegasi b around a solar-type star (Mayor & Queloz 1995) suggested that giant planets could form just as easily around late-type stars. The pace of planet detections around M dwarfs, however, remained much behind that around FGK stars, and giant planets appear to have a decreasing occurrence rate with decreasing stellar mass (Endl et al. 2006; Johnson et al. 2007; Bonfils et al. 2005).

Probing the whole sky for transiting planets, the Transiting Exoplanet Survey Satellite (TESS; Ricker et al. 2015) survey vastly expanded the target list and therefore was better able to detect rare outcomes of planet formation. A new planet population emerged: giant planets around very low-mass stars (e.g. TOI-519 b, Kagetani et al. 2023; TOI-3714 b, Cañas et al. 2022; TOI-3757 b, Kanodia et al. 2022; TOI-5205 b, Kanodia et al. 2023; and TOI-3235 b, Hobson et al. 2023). These planets are massive in comparison to expectations for protoplanetary disk masses around M dwarfs (Andrews et al. 2013; Gaidos 2017) and therefore are interesting for the investigation of planetary formation.

Recently, Bryant et al. (2023) performed a systematic search in the TESS photometry for giant planets transiting M dwarfs and measured an occurrence rate of 0.194 ± 0.072% giant planets with periods below 10 days per M dwarf (0.08−0.71 $M_\odot$), and 0.134 ± 0.069% for stellar masses between 0.088 and 0.4 $M_\odot$. Gan et al. (2023), also using the TESS data, measured a hot Jupiter occurrence rate around early-type M dwarfs (0.45−0.65 $M_\odot$) of 0.27 ± 0.09%. For comparison, the hot Jupiter occurrence rate around G-type stars is 0.55 ± 0.14% (Beleznay & Kunimoto 2022). Further characterisation of these planets' masses, orbits, and general architecture is now key to understanding how they form.

We report here the confirmation and mass measurement of TOI-4860 b[1]. Ground-based photometry confirms that the transits around TOI-4860, initially identified by TESS photometry, are produced by a giant planet. Doppler spectroscopy measures its mass and helps characterise the host star. This new planet detection adds to a small set of giant planets detected around stars with $M_\star$ < 0.4 $M_\odot$, a stellar mass regime where standard core accretion models are not able to form giants (e.g.

[1] We would like to acknowledge that another team has also conducted work on TOI-4860, utilising the same TESS data. Both teams made a mutual decision to submit our papers simultaneously, without discussing our respective findings. Therefore, both the current paper and the one by Triaud et al. (2023) present completely independent analyses of TOI-4860.

Burn et al. 2021), and therefore provides a challenge to the hypothesis underlying these models. Additionally, TOI-4860 b is an interesting target for atmospheric characterisation with transmission spectroscopy.

In Sect. 2, we describe the data used to detect and characterise TOI-4860 b. In Sect. 3, we characterise its host star, and in Sect. 4 we model the radial velocity (RV) and transit data. Finally, in Sect. 5 we discuss the results of our work.

2. Observations

2.1. TESS photometry

TOI-4860 was observed in four TESS sectors: one sector during the primary mission (sector 10, March and April 2019), two sectors during the first extended mission (sector 36, March and April 2021; sector 46, December 2021), and one sector in the second extended mission (sector 63, March and April 2023). Only full frame image (FFI) data were collected for sectors 10, 36, and 46, at respectively 30 min, 10 min, and 10 min cadence. For sector 63, data were obtained as both postage stamps at a 2-min cadence and 200-s FFIs.

A transit signature with a 1.52-days period and 6% depth was first identified from the FFIs by the Faint Star Search (Kunimoto et al. 2022) using data products from the Quick-Look Pipeline (QLP; Huang et al. 2020a,b; Kunimoto et al. 2021). The TESS Science Processing Operations Center (SPOC; Jenkins et al. 2016; Caldwell et al. 2020) at NASA Ames Research Center conducted a transit search of sector 36 on 5 May 2021 on an FFI 10-min cadence observation with an adaptive, noise-compensating matched filter (Jenkins 2002; Jenkins et al. 2010, 2020), producing a threshold crossing event for which an initial limb-darkened transit model was fitted (Li et al. 2019) and a suite of diagnostic tests were conducted to help make or break the planetary nature of the signal (Twicken et al. 2018). The signature and associated diagnostics were reviewed by the TESS Science Office and TOI-4860.01 was alerted as a TESS Object of Interest (TOI) on 21 December 2021 (Guerrero et al. 2021). The signal was repeatedly recovered as additional observations were made in sectors 46 and 63, and the transit signature passed all the diagnostic tests presented in the data validation reports. The difference image centroiding analyses constrain the location of the host star to within $3.5 \pm 2.5''$ of the source of the transit signal.

For the analysis in Sect. 4, we used the Presearch Data Conditioning Simple Aperture Photometry (PDCSAP; Smith et al. 2012; Stumpe et al. 2012, 2014; Caldwell et al. 2020) light curve of TOI-4860 (Fig. 1), produced by the SPOC, which is corrected for dilution in the TESS aperture by known contaminating sources. This is critical to ensure that no visually close-by targets that could affect the depth of the transit are present in the $21''$ TESS pixel and to check for a contaminating eclipsing binary. Figure 2 shows a plot of the target pixel file (TPF) from sector 10 and the aperture mask that is used for the simple aperture photometry (SAP). We can see that no star overlaps the TESS aperture down to six magnitudes fainter than TOI-4860.

2.2. Inspection for contaminants

2.2.1. Proper motion

TOI-4860 has a proper motion of 177 mas/yr (Gaia Collaboration 2023), and therefore has moved by $12''$ from its position on the Palomar Observatory Sky Survey (POSS; Minkowski & Abell 1963; Lasker et al. 1996) I red plate taken in 1954. This offset is large enough to check for background stars at the current position of TOI-4860, and we see none (Fig. 3).

2.2.2. *Gaia* assessment

In addition to proper motion, we used *Gaia* (Gaia Collaboration 2016, 2023) to identify any wide stellar companions that may be bound members of the system. Typically, these stars are already in the TESS Input Catalog (Stassun et al. 2019) and their flux dilution to the transit has already been accounted for in the transit fits and associated derived parameters. There are no additional widely separated companions identified by *Gaia* that have the same distance and proper motion as TOI-4860 (see also Mugrauer & Michel 2020, 2021).

The *Gaia* Data Release 3 (DR3) astrometry provides additional information on the possibility of inner companions that may have gone undetected by either *Gaia* or high-resolution imaging. The *Gaia* re-normalised unit weight error (RUWE) is a metric similar to a reduced chi-square, and values $\lesssim 1.4$ indicate that the *Gaia* astrometric solution is consistent with the star being single, whereas RUWE values $\gtrsim 1.4$ indicate excess astrometric noise, which is often caused by an unseen companion (e.g. Ziegler et al. 2020). TOI-4860 has a *Gaia* DR3 RUWE value of 1.04 and therefore appears single. Additionally, TOI-4860 does not appear in the *Gaia* DR3 non-single stars table (Gaia Collaboration 2022); as such, the *Gaia* astrometric fit is fully consistent with a single-star model.

2.2.3. High-resolution imaging

As part of our standard process for validating transiting exoplanets to assess the possible contamination of bound or unbound companions on the derived planetary radii (Ciardi et al. 2015), we also observed TOI-4860 with high-resolution near-infrared adaptive optics (AO) imaging at Keck Observatory. The observations were made with the Near Infra Red Camera 2 (NIRC2) instrument on Keck-II behind the natural guide star AO system (Wizinowich et al. 2000) on 10 June 2023 UT in the standard three-point dither pattern that is used with NIRC2 to avoid the left-lower quadrant of the detector, which is typically noisier than the other three quadrants. The dither pattern step size was $3''$ and was repeated twice, with each dither offset from the previous dither by $0.5''$. NIRC2 was used in the narrow-angle mode with a full field of view of $\sim 10''$ and a pixel scale of approximately $0.0099442''$ per pixel. The Keck observations were made in both the K_s filter ($\lambda_o = 2.146$; $\Delta\lambda = 0.311$ µm) and J ($\lambda_o = 1.248$; $\Delta\lambda = 0.163$ µm) with an integration time in each filter of 20 and 40 s for a total of 180 and 360 s, respectively. Flat fields were generated from a median average of dark subtracted dome flats. Sky frames were generated from the median average of the nine dithered science frames; each science image was then sky-subtracted and flat-fielded. The reduced science frames were combined into a single combined image using a intra-pixel interpolation that conserves flux, shifts the individual dithered frames by the appropriate fractional pixels; the final resolution of the combined dithers was determined from the full-width half-maximum of the point spread function; $0.101''$ and $0.114''$ for the two filters, respectively. To within the limits of the AO observations, no stellar companions were detected. The final 5σ limit at each separation was determined from the average of all of the determined limits at that separation and the uncertainty on the limit was set by the root mean square (RMS) dispersion of the azimuthal slices at a given radial distance (Fig. 4).

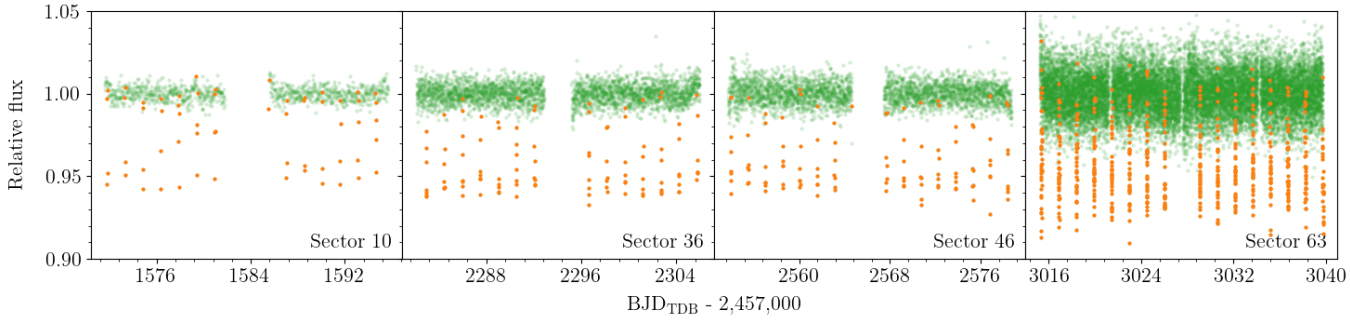

Fig. 1. TESS PDCSAP photometry time series (sectors 10, 36, 46, and 63; green dots), with the transits of TOI-4860 b highlighted in orange. The sampling is 30 min for sector 10, 10 min for sectors 36 and 46, and 2 min for sector 63.

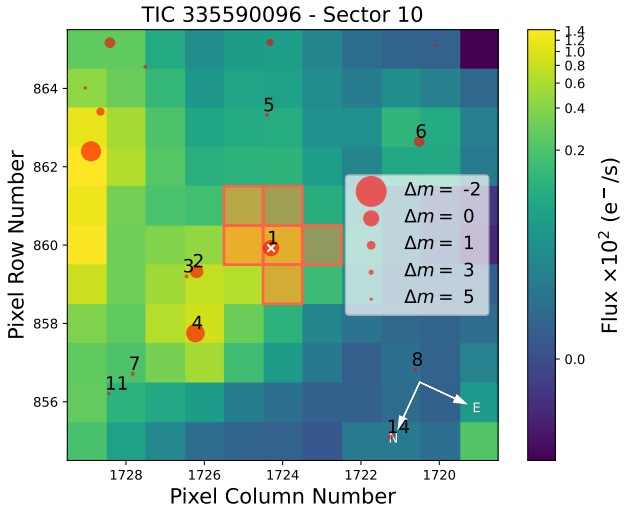

Fig. 2. TESS TPF image of TOI-4860 in sector 10 (created with `tpfplotter`; Aller et al. 2020). The electron counts are colour-coded. The red-bordered pixels are used in the SAP. The size of the red circles indicates the *Gaia* Data Release 2 magnitudes of all nearby stars (Gaia Collaboration 2018).

2.3. Ground-based photometry with ExTrA

Exoplanets in Transits and their Atmospheres (ExTrA; Bonfils et al. 2015) is a near-infrared (0.85 to 1.55 µm) multi-object low-resolution spectrograph fed by three 60 cm telescopes located at La Silla Observatory in Chile. One partial and six full transits were observed using two or three of the ExTrA telescopes. The first of those transits happened to be partial due to the then uncertain ephemeris, and helped refine the ephemeris for the following observations.

We used 8″ aperture fibres and the lowest-resolution mode (R~20) of the spectrograph, a combination that is optimal for the target's magnitude, with an exposure time of 60 s. Five fibres are positioned in the focal plane of each telescope to select light from the target and four comparison stars. We chose comparison stars[2] with 2-Micron All-Sky Survey (2MASS) J magnitudes (Skrutskie et al. 2006) and effective temperatures (Gaia Collaboration 2018) similar to the target. The resulting ExTrA data were analysed using a custom data reduction software, described in more detail in Cointepas et al. (2021).

[2] 2MASS J12145957-1303121, 2MASS J12154216-1243286, 2MASS J12130766-1243315, and 2MASS J12123143-1255153.

2.4. Radial velocities

2.4.1. SPIRou

The SPectropolarimètre InfraROUge (SPIRou) instrument is a near-infrared high-resolution (980–2450 nm; R = 70 000) high-stability (~1 m s^{-1}) velocimeter and spectropolarimeter installed at the Cassegrain focus of the 3.6 m Canada-France-Hawaii Telescope (CFHT) at Mauna Kea (Donati et al. 2020). TOI-4860 was observed between March 2022 and July 2023 with SPIRou as part of the large programme SPIRou Legacy Survey (SLS; ID P42, PI: Jean-François Donati). It was observed at 28 observing epochs with four polarimetric exposures per epoch, except on 4 July 2023 when the sequence was interrupted after the first exposure. In total, 109 spectra were acquired with integration time changing from 184 s for the first 8 exposures to 602 s for the rest of the sequence. The median signal-to-noise ratio (S/N) per pixel measured in the middle of the H band for the two exposure times were 9 and 28, respectively.

To process the raw data obtained with SPIRou, we employed A PipelinE to Reduce Observations (`APERO`; Cook et al. 2022) version 0.7.275. The `APERO` software initially corrects detector effects, removes constant background thermal components, and detects bad pixels and cosmic-ray impacts. Subsequently, it calculates the position of echelle spectral orders and optimally extracts spectra from fibres A, B, A+B, and C into 2D order-separated e2ds[3] and 1D order-merged s1d spectra. For the RV analysis, we use the A+B extraction (i.e. the combined extraction of the A and B science channels). A blaze function is derived from flat-field exposures. The wavelengths of the spectra are determined from a set of nightly calibrations following Hobson et al. (2021). An absolute calibration of wavelengths with respect to the Solar System barycentric rest frame is also performed using the current barycentric Earth radial velocity (BERV) and the barycentric Julian date (BJD) of each exposure with the `barycorrpy` code (Kanodia & Wright 2018; Wright & Eastman 2014). Finally, `APERO` applies a three-step telluric correction that we summarise here with a complete description to come (Artigau et al. in prep.). First, the extracted spectrum is pre-cleaned by fitting a TAPAS atmospheric model (Bertaux et al. 2014). Second, an empirical removal of residuals left after step one is performed using observations of fast-rotating hot stars observed with SPIRou at varying conditions (e.g. airmass and water column). Third, finite resolution artefacts from telluric modelling (Wang et al. 2022) are mitigated, leaving final residuals at the level of the Artigau et al. (2014) principal component analysis method.

[3] Extracted 2-dimensional spectrum.

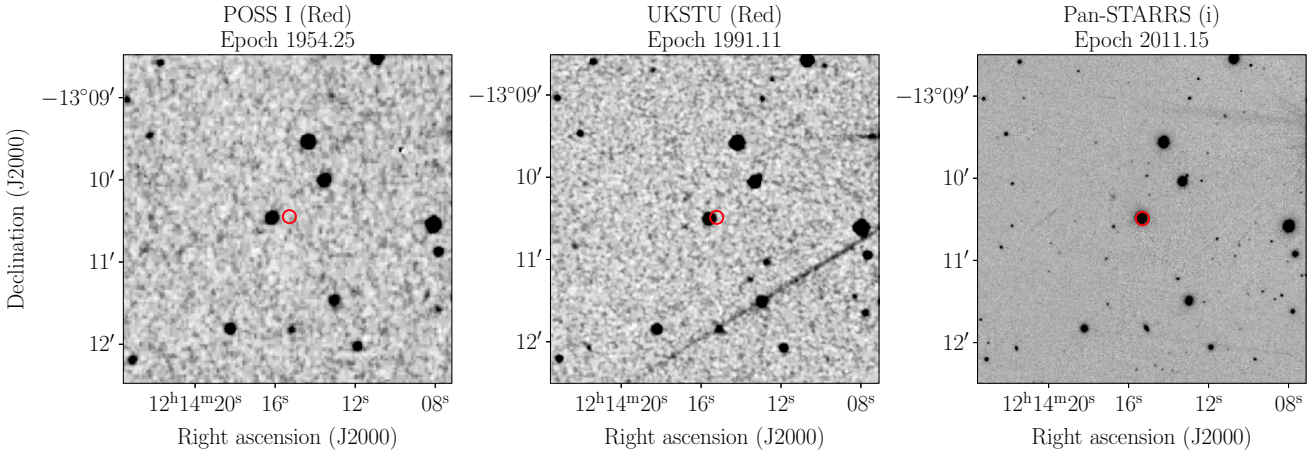

Fig. 3. Images extracted from the Digitized Sky Survey (DSS; retrieved from `https://archive.stsci.edu/cgi-bin/dss_form`) and the Pan-STARRS survey (Chambers et al. 2016). From left to right, the epochs are years 1954, 1991, and 2011. The open red circle marks the position of the star as determined by *Gaia* (Gaia Collaboration 2023). There is no background star at the current position of TOI-4860.

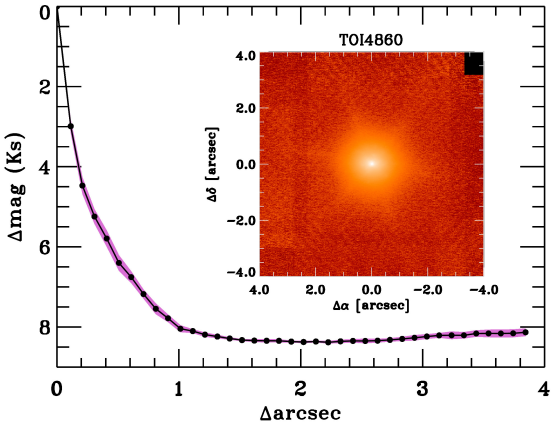

Fig. 4. Companion sensitivity for the near-infrared AO imaging. The black points represent the 5σ limits and are separated in steps of one full width at half maximum; the purple represents the azimuthal dispersion (1σ) of the contrast determinations (see the main text). The inset image is of the primary target and shows no additional close-in companions.

The line-by-line (LBL) method of Artigau et al. (2022) was then applied to the telluric-corrected spectra of TOI-4860 to measure its RVs. Several other TESS exoplanets were characterised with SPIRou using the LBL method in recent years: TOI-1759 b (Martioli et al. 2022), TOI-2136 b, (Gan et al. 2022), TOI-1452 b (Cadieux et al. 2022), and TOI-1695 b (Kiefer et al. 2023). The LBL method is a statistical framework where the RV is obtained from the weighted average of thousands of independent velocity measurements on individual spectral lines over the full wavelength domain. Velocities are derived from the difference between the observations and a high-S/N template spectrum of the star (Bouchy et al. 2001 formalism). In practice, one can use the template of any similar spectral type star in the LBL calculation. Since TOI-4860 is relatively faint, we chose to use instead the template of Gl 905, a bright M5V star observed in the SLS over 3 yr. The final RVs are presented in Table A.2 and have median uncertainties of respectively 34.3 m s^{-1} and 16.2 m s^{-1} for the 184 s and 602 s exposures.

The TOI-4860 SPIRou observations were performed in circular polarisation mode (Stokes V), where each visit consists of a set of four exposures that provide a polarimetric spectrum. We used previously described methods (Donati et al. 1997; Martioli et al. 2020, 2022; Cook et al. 2022), implemented in the `APERO` pipeline, to calculate the polarimetric spectra of TOI-4860 and analyse the Stokes V spectra using least squares deconvolution technique as in Donati et al. (1997). With a typical S/N of only 30 to 40, and even using least squares deconvolution analysis, we obtained a mean polarimetric RMS per visit of $\sigma_V = 0.2 \pm 0.1\%$. Such precision is sensitive to a disk-integrated longitudinal magnetic field on the stellar surface of the order of $B_\ell > 20$ G. Non-detections suggest that TOI-4860 is not extremely active, but moderate magnetic activity cannot be completely ruled out.

2.4.2. ESPRESSO

We obtained seven spectra of TOI-4860 with the Echelle SPectrograph for Rocky Exoplanets and Stable Spectroscopic Observations (ESPRESSO; Pepe et al. 2021) at the 8.2 m ESO Very Large Telescope (VLT) array, at the Paranal Observatory in Chile. The observations were obtained from January to February 2023 in Programme ID: 0110.C-4069 (PI: Jordán) as part of a long-running campaign to obtain mass measurements for giant planets transiting low-mass host stars. Initially, candidates for this campaign were drawn from the HAT-South survey (Bakos et al. 2013), and more recently from the TOI list (Guerrero et al. 2021) and our own dedicated search of the TESS FFI data (Bryant et al. 2023).

We observed TOI-4860 in the single Unit Telescope (UT), high-resolution (HR) mode (1″ fibre, $R \sim 140\,000$) over a spectral range from ~380 to ~780 nm. The spectrograph is contained in a temperature- and pressure-controlled vacuum vessel to avoid spectral drifts, and records cross-dispersed echelle spectra on two detectors. They were read out in the 2×1 binned mode, which presents a reduced level of continuum noise as compared to the unbinned readout mode. The calibration fibre (fibre B) was placed on sky in order to monitor and remove any possible contamination from the moon, as well as any sky emission lines.

The recorded spectra have a median S/N value of ~8 at 550 nm, with this value rising to ~25 towards the red end of the spectrum. The spectra were reduced with the updated version of the dedicated Data Reduction Software (`DRS; v. 3.0.0`), which, among other improvements, mitigates the bug in the exposure-meter data tables that affects the flux-weighted mid-exposure time calculation. The reduction includes

all the standard steps, whereby the pipeline provides RV measurements by fitting a Gaussian function to the measured cross-correlation function (CCF; Baranne et al. 1996; Pepe et al. 2002). This CCF is calculated using a stellar template matching closest the spectral type of the star (M4 in this case). The measured RVs are given in Table A.2.

3. Stellar parameters

TOI-4860 is an M-type star located at a distance of 80.42 ± 0.22 pc (Gaia Collaboration 2016, 2023; Lindegren et al. 2021). The astrometry, photometry, and stellar parameters are reported in Table 1.

We derived the mass and radius of TOI-4860 from empirical relations based on luminosity. We used the *Gaia*-corrected (Gaia Collaboration 2016, 2023; Lindegren et al. 2021) parallax determination (12.43 ± 0.03 mas) to compute the distance and an absolute magnitude of $M_{K_s} = 6.648 \pm 0.027$. We then used the empirical relations of Mann et al. (2019) and Mann et al. (2015) with the metallicity dependence to derive a mass of $M_\star = 0.340 \pm 0.009\ M_\odot$ and a radius of $R_\star = 0.358 \pm 0.015\ R_\odot$, respectively. For the stellar radius, we used a systematic uncertainty floor of 4% following Tayar et al. (2022). We derived an alternate stellar radius from the spectral energy distribution (SED) that we constructed using the magnitudes from *Gaia* (Riello et al. 2021), 2MASS (Skrutskie et al. 2006; Cutri et al. 2003), and the Wide-field Infrared Survey Explorer (WISE; Wright et al. 2010; Cutri et al. 2013). Those measurements are listed in Table 1. We modelled these magnitude measurements using the procedure described in Díaz et al. (2014), with the PHOENIX/BT-Settl (Allard et al. 2012) stellar atmosphere models. We used informative priors for the effective temperature ($T_{\rm eff} = 3190 \pm 70$ K), and metallicity ([Fe/H] = 0.27 ± 0.12 dex) derived from the co-added ESPRESSO spectra (which we analysed with `SpecMatch-Emp`; Yee et al. 2017), and for the distance from *Gaia*. We used uniform priors for the rest of the parameters. We used a jitter (Gregory 2005) for each set of photometric bands (*Gaia*, 2MASS, and WISE). The parameters, priors, and posteriors are listed in Table A.1. The maximum a posteriori (MAP) model is shown in Fig. 5. The derived SED radius ($R_\star = 0.371 \pm 0.010\ R_\odot$) is compatible ($0.7\sigma$) with the radius computed above using an empirical radius-luminosity relation. The derived SED $T_{\rm eff} = 3260 \pm 50$ K, which corresponds to an M3.5V spectral type (Pecaut & Mamajek 2013), is our adopted value.

The flux around the calcium lines is low but using the co-added ESPRESSO spectra, we were able to measure the value of $\log R'_{HK} = -5.65 \pm 0.12$, derived from the calcium doublet. This translates to an estimated stellar rotation period of $P_{\rm rot} = 114 \pm 22$ days using the activity-rotation relation of Astudillo-Defru et al. (2017). Such a rotation period falls within the distribution of the 'slow-rotator' population of mid-M-type dwarfs in the field (Newton et al. 2017; Kiman et al. 2021; Popinchalk et al. 2021); thus, the star is likely in the Skumanich-like spin-down phase, in which the braking law is strongly rotation-dependent and the period is a predictor of age. The effective temperature of TOI-4860 (3260 K) is at the poorly constrained cool end of the 4 Gyr gyrochronology calibration based on rotation periods of M67 M dwarf cluster members (Dungee et al. 2022; Gaidos et al. 2023), but adopting this yields an age of ∼2.2 Gyr. The star could be older if it has gained angular momentum from the close-in planet via tides and is more rapidly rotating and active as a result (Ilic et al. 2022).

Table 1. Stellar parameters for TOI-4860 (TIC 335590096, UCAC4 385-060574, 2MASS J12141555-1310290, WISE J121415.40-131029.3, *Gaia* DR3 3571038605366263424).

Parameter	Value	Refs
Astrometry		
Right ascension (J2016), α	$12^{\rm h}14^{\rm m}15.34^{\rm s}$	1
Declination (J2016), δ	$-13°10'29.43''$	1
Parallax, π (mas)	12.43 ± 0.03	1,2
Distance, d (pc)	80.42 ± 0.22	1,2
Proper motion α (mas yr^{-1})	−177.24 ± 0.04	1
Proper motion δ (mas yr^{-1})	−5.43 ± 0.03	1
Photometry		
V (mag)	16.47 ± 0.02	3
Gaia-BP (mag)	16.7328 ± 0.0074	1
Gaia-G (mag)	15.0774 ± 0.0030	1
Gaia-RP (mag)	13.8435 ± 0.0033	1
TESS magnitude (mag)	13.7726 ± 0.0079	3
J (mag)	12.056 ± 0.022	4
H (mag)	11.431 ± 0.026	4
K_s (mag)	11.175 ± 0.026	4
WISE-$W1$ (mag)	11.016 ± 0.023	5
WISE-$W2$ (mag)	10.886 ± 0.020	5
WISE-$W3$ (mag)	10.96 ± 0.14	5
Stellar parameters		
Spectral type	M3.5	6
M_{K_s} (mag)	6.648 ± 0.027	1,2,4,7
Stellar radius, $R_\star$ ($R_\odot$)	0.358 ± 0.015	7,8
Stellar mass, $M_\star$ ($M_\odot$)	0.340 ± 0.009	7,9
Effective temperature, $T_{\rm eff}$ (K)	3260 ± 50	7, SED
Surface gravity, $\log g$ (cgs)	4.86 ± 0.04	$R_\star$, $M_\star$
Metallicity, [Fe/H] (dex)	0.27 ± 0.12	7,10
$\log R'_{HK}$	−5.65 ± 0.12	7

References: (1) Gaia Collaboration (2023), (2) Lindegren et al. (2021), (3) Stassun et al. (2019), (4) Cutri et al. (2003), (5) Cutri et al. (2013), (6) Pecaut & Mamajek (2013), (7) This work, (8) Mann et al. (2015), (9) Mann et al. (2019), (10) Yee et al. (2017).

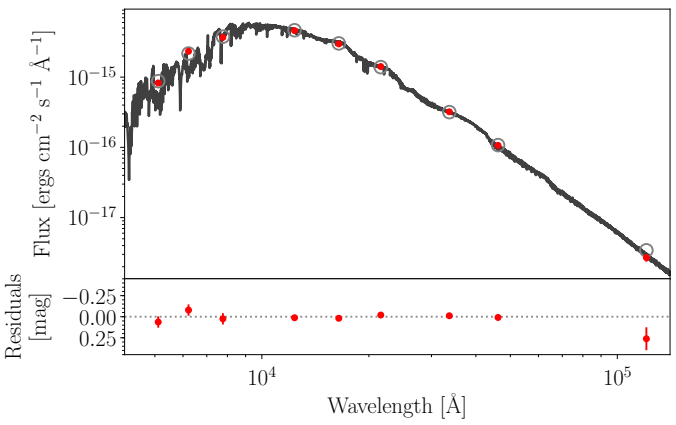

Fig. 5. SED of TOI-4860. The solid line is the MAP PHOENIX/BT-Settl-interpolated synthetic spectrum, red circles are the absolute photometric observations (the jitter has been added quadratically to the data error bars), and grey open circles are the result of integrating the synthetic spectrum into the observed bandpasses.

Table 2. Inferred $R_p/R_\star$ in different bands.

Band	λ_{pivot} (nm)	Prior	Median and 68.3% CI
TESS	769.8	$U(0.1, 0.3)$	$0.2202^{+0.0027}_{-0.0030}$
ExTrA	1165.4	$U(0.1, 0.3)$	$0.2204^{+0.0025}_{-0.0028}$
ExTrA Z^*	889.8	$U(0.1, 0.3)$	$0.2174^{+0.0034}_{-0.0036}$
ExTrA Y	1030.5	$U(0.1, 0.3)$	$0.2190^{+0.0029}_{-0.0031}$
ExTrA J	1248.3	$U(0.1, 0.3)$	$0.2192^{+0.0027}_{-0.0029}$
ExTrA H^*	1526.4	$U(0.1, 0.3)$	$0.2220^{+0.0041}_{-0.0042}$

Notes. The table lists: band, λ_{pivot} (Koornneef et al. 1986), prior, posterior median, and 68.3% CI. $U(a, b)$: A uniform distribution defined between a lower a and an upper b limit.

4. Analysis and modelling

We used the software package `juliet` (Espinoza et al. 2019) to model the photometric and RV data. The algorithm is built on many publicly available tools for the modelling of transits (`batman`, Kreidberg 2015), RVs (`radvel`, Fulton et al. 2018), and Gaussian processes (GPs; `george`, Ambikasaran et al. 2015; `celerite`, Foreman-Mackey et al. 2017). In order to compare different models, `juliet` efficiently computes the Bayesian evidence ($\mathcal{Z}$) using `dynesty` (Speagle 2020), a python package to estimate Bayesian posteriors and evidence using nested sampling methods. Instead of starting with an initial parameter vector centred on a likelihood maximum discovered through optimisation techniques, nested sampling algorithms sample directly from the given priors.

4.1. Transit chromaticity with TESS and ExTrA photometry

A wavelength-dependent transit depth would suggest a false positive scenario involving an eclipsing binary. We therefore performed a joint fit of both TESS and ExTrA photometry. To push further the chromatic analysis, in addition to ExTrA's full wavelength range (0.85 to 1.55 µm) light curve, we synthesised from the ExTrA spectrophotometry photometry in the UKIRT-WFCAM filters,[4] to produce four additional light curves: a truncated Z band (Z^*), a Y, a J, and a truncated H band (H^*), shown in Fig. A.1. The analysis is similar to that presented in Sect. 4.4 except that RVs are not used and the eccentricity is fixed to zero. All planetary parameters except for the planet-to-star radius ratio ($R_p/R_\star$) are common to all datasets, to allow for a different transit depth at each band, whose posteriors' median and 68.3% credible interval (CI) are listed in Table 2. As shown in Fig. 6 the photometry for all of these bandpasses is consistently modelled with a similar $R_p/R_\star$. No chromaticity is seen, lending confidence in the planet detection rather than a scenario with a blended binary[5].

4.2. Transit timing variations

Transit timing variations (TTVs) would indicate the presence of additional planets (Agol et al. 2005; Holman & Murray 2005) or orbital decay (Patra et al. 2017). We analysed the TESS and ExTrA transit photometry with two models: one with a linear ephemeris and a second that allows for the time of individual transits to vary (with uniform priors of ±10 min width around the linear ephemeris of the first model). The resulting TTVs are shown in Fig. A.2. A model comparison strongly favours (Kass & Raftery 1995) the model with a linear ephemeris (P, T_0) over the one with TTVs (log-Bayes factor $\mathcal{Z}_{P,T_0}/\mathcal{Z}_{\rm TTVs}$ of 92.5 ± 0.8).

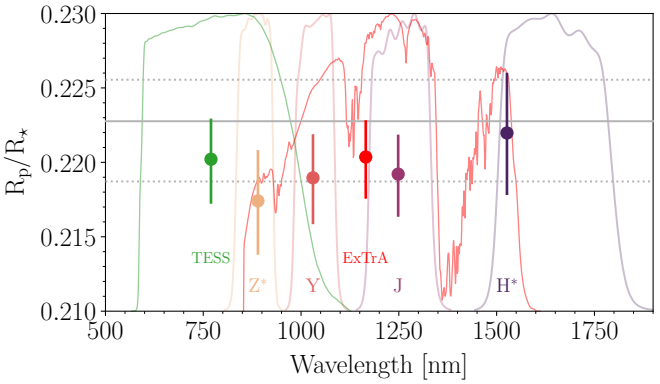

Fig. 6. Posterior distribution comparison for $R_p/R_\star$ (error bars) computed for different bands (shown and labelled with different colours). TESS, ExTrA (0.85–1.55 µm), Z^*, Y, J, and H^* data are fitted jointly with a different $R_p/R_\star$ parameter for each of the datasets. The horizontal solid and dotted grey lines represent the posterior median and 68.3% CI of $R_p/R_\star$ inferred in Sect. 4.4.

4.3. Radial velocity

The RVs are listed in Table A.2. One ESPRESSO and six SPIRou observations were taken during transit. The $\log R'_{HK}$ is indicative of a slow rotator, which would imply a Rossiter-McLaughlin effect (Rossiter 1924; McLaughlin 1924) semi-amplitude of just ∼5 m s^{-1} (based on $P_{\rm rot}$, estimated from the $\log R'_{HK}$, we computed a $v \sin i_\star$ of ∼160 m s^{-1}, assuming $i_\star = 90°$). Except for in regards to the discussion on a potential system misalignment (Sect. 5, Fig. A.4), we excluded the ESPRESSO measurement taken during the transit from our analyses. However, we included the SPIRou measurements taken during the transit in all our analyses, as the expected amplitude of the Rossiter-McLaughlin effect is smaller than their accuracy. For the SPIRou data, we used the nightly weighted average (we excluded the spectra on BJD 2460096.806090 because it is an outlier, and BJD 2460064.896367 and 2460064.903591 because of a low S/N of about 2.5 in the middle of the H band). We first analysed the RV data alone to choose the model for the RVs in the global fit.

Figure A.3 shows the periodogram of SPIRou RVs, whose highest peak corresponds to the period of TOI-4860 b. The residuals, after the signal from TOI-4860 b has been removed, exhibit additional signals over a longer timescale. This finding is also supported by the ESPRESSO data, for which a model with a circular planet (with priors on ephemeris from the transit observations) and a drift in RV are strongly favoured relative to the same model without drift (log-Bayes factor of 3.9 ± 0.3). We conducted a joint modelling of the SPIRou and ESPRESSO data to search for a second planet. We assumed a circular orbit for the transiting planet, and added a Keplerian with a period range between 10 and 1000 days. The marginal posterior distribution of the trial period shows a peak at 427 days (see Fig. A.3). The log-Bayes factor for this model with respect to the one-planet model is 12.3 ± 0.4, which can be interpreted as very strong evidence in

[4] Retrieved from the SVO Filter Profile Service (`http://svo2.cab.inta-csic.es/theory/fps/`, Rodrigo et al. 2012; Rodrigo & Solano 2020).

[5] An equivalent analysis was done with just the first full ExTrA transit and the first two TESS sectors prior to the acquisition of RV observations.

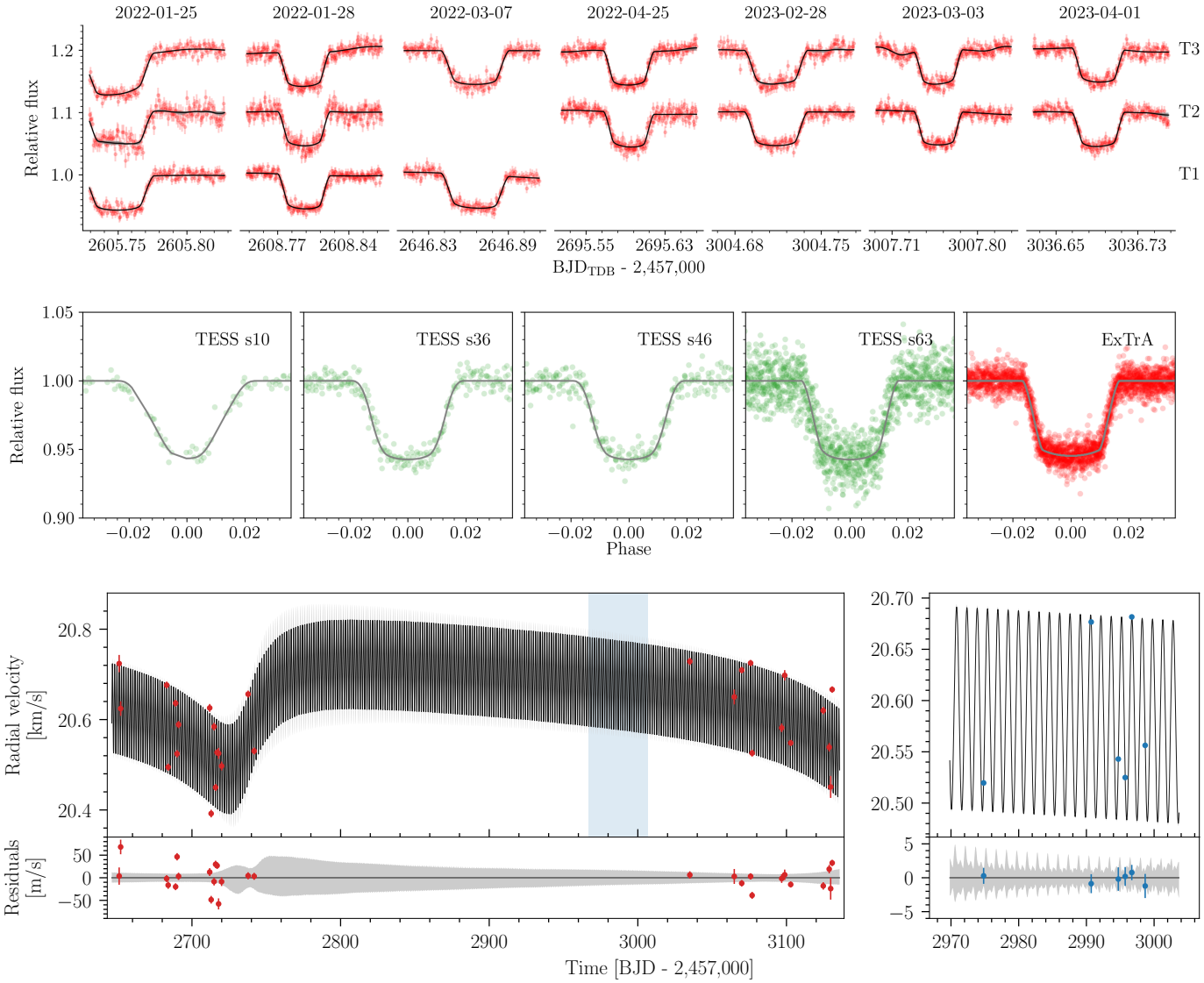

Fig. 7. Modelling of transit photometry and RVs of TOI-4860. *Top panel*: ExTrA transit photometry observations of TOI-4860 b. Each column corresponds to a night (labelled with format YYYY-MM-DD) and each line to an ExTrA telescope (labelled T1, T2, and T3) that is offset vertically for clarity. For each transit, the median model (black line) and the 68% CI (grey band, barely visible) computed from 1000 random posterior samples are shown. *Middle panel*: TESS (separated by sector) and ExTrA transits detrended with the MAP model (whose transit component is shown as a grey line) and phase-folded. TESS sector 10 looks more V-shaped due to the 30-min sampling. *Bottom-left panel*: SPIRou RVs (red error bars), median model (black line), and 68% CI (grey band). Residuals from the median model are shown. *Bottom-right panel*: same as the bottom-left panel but for ESPRESSO RVs (blue error bars). The time span of the ESPRESSO panel is highlighted as a blue band in the SPIRou panel.

favour of a second planet in the system (planet c candidate). We therefore used a model with two Keplerians for the joint fit of transit photometry and RVs. To confirm whether the additional signal in the RVs corresponds to a second planet in the system, more data are needed. The current time-span of 480 days is too close to the proposed period, and there is poor phase coverage.

The posterior of the SPIRou jitter in the two-planet modelling is 27 ± 6 m s^{-1}, doubling the SPIRou uncertainties. This jitter is probably inherent to the SPIRou data since the ESPRESSO data do not support it.

4.4. Joint fit of all data

We conducted an analysis of the transit photometry from TESS (data were extracted around three transit durations at the centre of each transit) and ExTrA (spanning the full wavelength range from 0.85 to 1.55 µm), as well as the RVs from SPIRou and ESPRESSO. A GP with an approximate Matern kernel was utilised to model the residuals in the transit photometry. Each transit observation had distinct kernel hyperparameters, except for the TESS data, where common kernel hyperparameters were used within each sector. For TESS sectors 10, 36, and 46, we over-sampled the model in time and adjusted for the observation's integration time through binning (Kipping 2010). The RV model comprised two Keplerians. We sampled from the posterior using `dynesty` (Speagle 2020). Table 3 presents the prior, median, and 68% CI of the marginal distributions of the inferred system parameters. The stellar mass and radius, as determined in Sect. 3, were used to calculate the planetary mass and radius of TOI-4860 b. Figures 7 and 8 display the datasets and the model

Table 3. Inferred system parameters.

Parameter	Units	Prior	Median and 68.3% CI
Star			
Mean density, $\rho_\star$	(g cm^{-3})	$U(5, 20)$	11.7 ± 0.8
q_1 TESS		$U(0, 1)$	$0.34^{+0.26}_{-0.16}$
q_2 TESS		$U(0, 1)$	$0.29^{+0.3}_{-0.17}$
q_1 ExTrA		$U(0, 1)$	$0.136^{+0.21}_{-0.09}$
q_2 ExTrA		$U(0, 1)$	$0.26^{+0.4}_{-0.19}$
Planet b			
Semi-major axis, a	(au)		0.01808 ± 0.00015
Eccentricity, e			$< 0.035^{(a)}$, $(0.008^{+0.013}_{-0.006})$
Argument of pericentre, ω	(°)		240 ± 130
Inclination, i_p	(°)		$88.5^{+0.6}_{-0.4}$
Radius ratio, $R_\mathrm{p}/R_\star$			$0.2228^{+0.0028}_{-0.004}$
Scaled semi-major axis, $a/R_\star$			11.0 ± 0.4
Impact parameter, b			$0.29^{+0.06}_{-0.11}$
Transit duration, T_{14}	(h)		1.231 ± 0.011
$T_0 - 2\,460\,000$	(BJD$_\mathrm{TDB}$)	$U(36.6907, 36.6918)$	36.69124 ± 0.00010
Orbital period, P	(days)	$U(1.522757, 1.522761)$	$1.5227591 \pm 3 \times 10^{-7}$
RV semi-amplitude, K	(m s^{-1})	$U(90, 110)$	98.9 ± 1.3
Radius, R_p	($\mathcal{R}^\mathrm{N}_{e\mathrm{E}}$)		8.7 ± 0.4
	($\mathcal{R}^\mathrm{N}_{e\mathrm{J}}$)		0.77 ± 0.03
Mass, M_p	($\mathrm{M_E}$)		86.7 ± 1.9
	(M_J)		0.273 ± 0.006
Mean density, ρ_p	(g cm^{-3})		0.75 ± 0.09
Surface gravity, $\log g_\mathrm{p}$	(cgs)		3.06 ± 0.03
Equilibrium temperature, T_eq	(K)		694 ± 15
Insolation flux	(F_E)		42.5 ± 1.9
r_1		$U(0, 1)$	$0.53^{+0.04}_{-0.07}$
r_2		$U(0.20, 0.24)$	$0.2228^{+0.0028}_{-0.004}$
$\sqrt{e}\cos\omega$		$U(-1, 1)$	-0.02 ± 0.06
$\sqrt{e}\sin\omega$		$U(-1, 1)$	-0.02 ± 0.10
Candidate planet c			
Semi-major axis, a	(au)		0.776 ± 0.011
Eccentricity, e			0.66 ± 0.09
Argument of pericentre, ω	(°)		222 ± 14
Scaled semi-major axis, $a/R_\star$			466 ± 22
$T_0 - 2\,460\,000$	(BJD$_\mathrm{TDB}$)	$U(-200, 350)$	92 ± 19
Orbital period, P	(days)	$U(350, 550)$	427 ± 7
RV semi-amplitude, K	(m s^{-1})	$U(0, 250)$	121 ± 27
Minimum mass, $M_\mathrm{p} \sin i$	(M_J)		1.66 ± 0.26
Equilibrium temperature, T_eq	(K)		107 ± 3
Insolation flux	(F_E)		0.0230 ± 0.0012
$\sqrt{e}\cos\omega$		$U(-1, 1)$	$-0.59^{+0.14}_{-0.09}$
$\sqrt{e}\sin\omega$		$U(-1, 1)$	-0.54 ± 0.18
RV			
SPIRou jitter	(m s^{-1})	$J(0.01, 80)$	27 ± 5
SPIRou offset	(m s^{-1})	$U(20\,500, 20\,800)$	20662 ± 16
ESPRESSO jitter	(m s^{-1})	$J(0.01, 10)$	$0.14^{+0.7}_{-0.12}$
ESPRESSO offset	(m s^{-1})	$U(20\,400, 20\,650)$	$20\,571 \pm 9$
Photometry			
Offset relative flux	(Relative flux)	$N(0, 0.01)$	$^{(b)}$
Jitter	(ppm)	$J(1, 1000)$	$^{(b)}$
Amplitude of the GP	(Relative flux)	$J(10^{-6}, 0.1)$	$^{(b)}$
Timescale of the GP	(days)	$J(0.001, 10)$	$^{(b)}$

Notes. The table lists: prior, posterior median, and 68.3% CI. Parameters without prior are derived parameters. $^{(a)}$Upper limit, 95% confidence. $^{(b)}$The parameters listed for the photometry are different for each TESS sector and for each individual transit observed with each of the telescopes of ExTrA. The parameters q_1 and q_2 are the quadratic limb-darkening coefficients parameterised using Kipping (2013). The parameters r_1 and r_2 are the impact parameter and transit depth parameterised using Espinoza (2018). The planetary equilibrium temperature is computed for zero albedo and full day/night heat redistribution. IAU 2012: au = 149 597 870 700 m. IAU 2015: $\mathcal{R}^\mathrm{N}_\odot = 6.957 \times 10^8$ m, $\mathcal{R}^\mathrm{N}_{e\mathrm{E}} = 6.378\,1 \times 10^6$ m, $(\mathcal{GM})^\mathrm{N}_\odot = 1.327\,124\,4 \times 10^{20}$ m^3 s^{-2}, $(\mathcal{GM})^\mathrm{N}_\mathrm{E} = 3.986\,004 \times 10^{14}$ m^3 s^{-2}, $\mathcal{R}^\mathrm{N}_{e\mathrm{J}} = 7.149\,2 \times 10^7$ m, $(\mathcal{GM})^\mathrm{N}_\mathrm{J} = 1.266\,865\,3 \times 10^{17}$ m^3 s^{-2}. $M_\odot = (\mathcal{GM})^\mathrm{N}_\odot/\mathcal{G}$, $\mathrm{M_E} = (\mathcal{GM})^\mathrm{N}_\mathrm{E}/\mathcal{G}$, $M_\mathrm{J} = (\mathcal{GM})^\mathrm{N}_\mathrm{J}/\mathcal{G}$. CODATA 2018: $\mathcal{G} = 6.674\,30 \times 10^{-11}$ m^3 kg^{-1} s^{-2}. $U(a, b)$: A uniform distribution defined between a lower a and an upper b limit. $J(a, b)$: Jeffreys (or log-uniform) distribution defined between a lower a and upper b limit. $N(\mu, \sigma)$: Normal distribution prior with mean μ, and standard deviation σ.

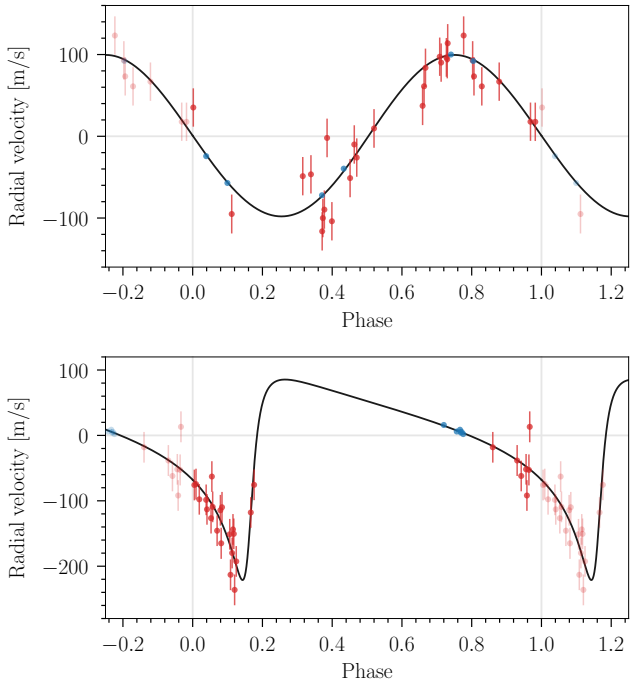

Fig. 8. Phased RVs. *Top panel*: SPIRou (red error bars) and ESPRESSO (blue error bars) RVs corrected for the MAP Keplerian orbit of planet c and phase-folded to the period of planet b (the MAP jitter has been added quadratically to the data error bars). The black line is the best-fit Keplerian model from the joint fit. *Bottom panel*: idem for the planet c candidate.

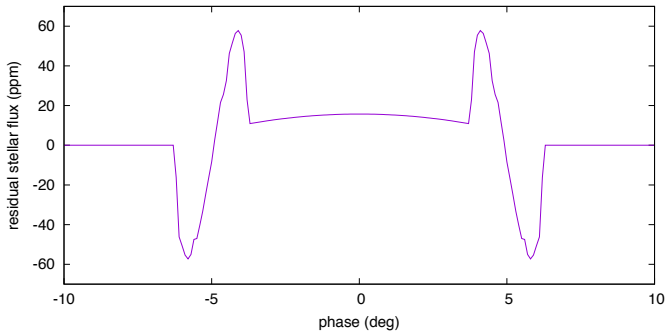

Fig. 9. Difference between the transit light curves of an ellipsoidal and a spherical planet for TOI-4860 b, obtained with uniform stellar flux.

derived from this analysis. The posterior of the stellar density (11.7 ± 0.8 g cm^{-3}) is consistent with the value derived from the stellar mass and radius in Sect. 3 (10.4 ± 1.5 g cm^{-3}).

We examined the transit windows of the candidate planet c over the span of available observations, and all of them fall at least 2σ away from a TESS sector. Additionally, we used `REBOUND` (Rein & Liu 2012) to estimate the TTVs of TOI-4860 b, due to the presence of the candidate planet c, for the median values of the posterior. The semi-amplitude of the TTVs is 1.6 s with a period corresponding to the candidate planet c, and is dominated by the light-time effect (Irwin 1952). This signal is well below the precision (18 or 56 s at best for a transit observed with ExTrA or TESS, respectively) and dispersion of the measured TTVs (Fig. A.2).

5. Results and discussion

In this paper we present the discovery and characterisation of a giant planet, TOI-4860 b, transiting an M3.5 dwarf with a period of 1.52 days. The exoplanet was detected by the TESS mission, then characterised from ground-based photometric follow-up using ExTrA and from precise RV measurements by both SPIRou and ESPRESSO.

The giant planet is close to its host star, at only 1.8 times the Roche limit (see Chandrasekhar 1987). Therefore, we expect that the system undergoes strong tidal interactions, which distort the planet and lead to orbital decay. Adopting a radial fluid Love number identical to that of Jupiter, $h_f = 1.5$, we estimate a difference between the longest and the shortest radius of the planet of about 3% (Correia 2014). In addition, since the planet's mean radius is about 22% of the stellar radius, we expect ~60 ppm discrepancies with respect to a spherical planet during transit ingress and egress (see Fig. 9). These variations are similar to those observed for WASP-103 b (Akinsanmi et al. 2019; Barros et al. 2022) and can thus be used to probe the interior structure of the planet using the transit light curves (Ragozzine & Wolf 2009; Correia 2014). The tidal dissipation of M-dwarf stars is unknown, but often believed to be similar to that of other convective stars (e.g. Mathis 2015). Assuming a tidal quality factor of $Q'_* = 10^5$, we estimate a variation in the orbital period of about $\dot{P} \sim 10^{-9}$ day yr^{-1} (Maciejewski et al. 2018). This rate is not detectable with current instrumentation, but a direct estimation of $\dot{P}$ can still be used to put a lower limit on the tidal Q factor of the star (e.g. Barros et al. 2022).

A long-standing prediction from core accretion planet formation is that giant planets do not form around low-mass stars (Laughlin et al. 2004). In particular, the models of Burn et al. (2021) are unable to form giant planets around stars with masses $M_* \lesssim 0.4\ M_\odot$. The lack of such systems from the first ground-based transit surveys, such as WASP (Pollacco et al. 2006; Gaidos et al. 2014) and HATNet (Bakos et al. 2004), seemed to confirm this prediction, although the magnitude range of these surveys meant very few low-mass stars were monitored to the precision needed to find transiting exoplanets. A new generation of ground-based transit surveys, with increased telescope apertures (e.g. HAT-South and NGTS; Bakos et al. 2013; Bayliss et al. 2018), began to find transiting gas giant planets around lower-mass stars (Hartman et al. 2015; Bayliss et al. 2018; Bakos et al. 2020; Jordán et al. 2022) but still not below the mass where core-accretion models have trouble forming giants. The TESS mission, with its near all-sky coverage and red wavelength sensitivity, is very well placed to detect giant planets transiting low-mass stars. This has allowed the discovery of transiting giants hosted by stars with masses $M_\star \lesssim 0.4\ M_\odot$ (TOI-5205, Kanodia et al. 2023; TOI-3235, Hobson et al. 2023; and TOI-519, Parviainen et al. 2021; Kagetani et al. 2023). The TOI-4860 system, an M3.5V star that hosts a giant planet with a radius of $0.77 \pm 0.03\ R_\mathrm{J}$ and a mass of $0.273 \pm 0.006\ M_\mathrm{J}$ (see Fig. 10) at the border of the hot Neptune desert (e.g. Lecavelier Des Etangs 2007), joins this short list of discoveries. With a mass of $0.340 \pm 0.009\ M_\odot$ and a radius of $0.358 \pm 0.015\ R_\odot$, its host star is well within the mass range that challenges core accretion.

These recent discoveries have allowed for the occurrence rates of giant planets around low-mass stars to be calculated, at least for short orbital period systems. The results from Gan et al. (2023) and Bryant et al. (2023) suggest that short-period giant planets occur around early-type M dwarfs at approximately half the frequency they do around solar-mass stars, and about a quarter the frequency when comparing mid to late M-dwarf hosts ($0.088-0.4\ M_\odot$), such as TOI-4860, to solar-mass stars. These

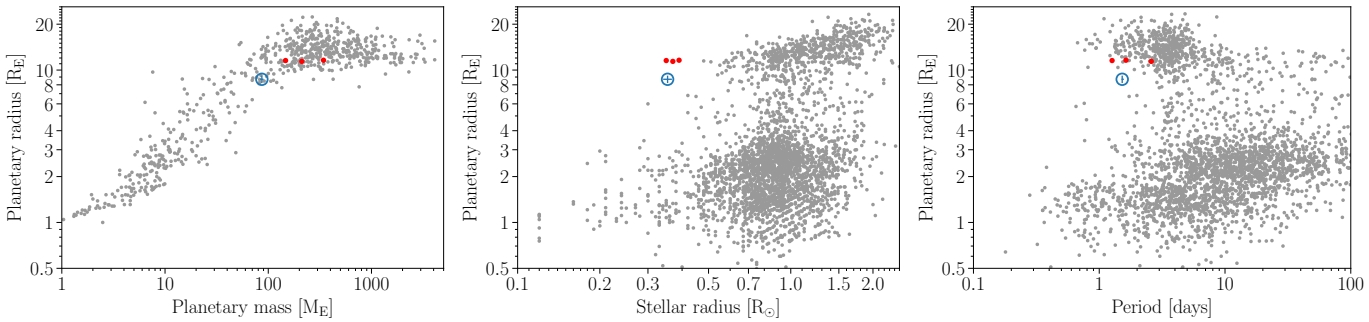

Fig. 10. Comparison of TOI-4860 b with known exoplanets. *Left*: mass–radius diagram of known exoplanets. Grey dots are transiting planets listed in the NASA Exoplanet Archive (https://exoplanetarchive.ipac.caltech.edu/) with planetary radius and mass uncertainties below 20%. TOI-519, TOI-3235, and TOI-5205 are shown (from left to right) as red dots. The blue open circle with error bars marks the position of TOI-4860 b. *Centre*: idem for planetary versus stellar radii (restricted to planets with planetary radius uncertainties below 20%). *Right*: idem for planetary radii versus orbital period.

results will become more concrete as more systems similar to TOI-4680 are confirmed.

TOI-4860 appears to be metal-rich ([Fe/H] = 0.27 ± 0.12), like other M dwarfs that host giant planets (see Fig. 3 of Kagetani et al. 2023). This suggests, as for FGK stars (Fischer & Valenti 2005), a correlation between the metallicity of a star and the likelihood of its hosting giant planets.

TOI-4860 b has a high transmission spectroscopy metric (Kempton et al. 2018) of 183 ± 15, among the highest for its planet size. Moreover, based on the host star's $\log R'_{HK}$ (−5.65 ± 0.12), the lack of flares in the TESS light curve, and the small ESPRESSO RV jitter (< 1.9 $m\,s^{-1}$ at 95% CI), we conclude that TOI-4860 currently exhibits low levels of activity. The planet's atmospheric composition can reveal insights into its formation and evolution history and is a key constraint for models of the planetary interior. Another constraint that can be placed upon the formation history could be the spin-orbit angle. The expected semi-amplitude of the Rossiter-McLaughlin effect (Rossiter 1924; McLaughlin 1924) for TOI-4860 b is ∼5 $m\,s^{-1}$, well above ESPRESSO capabilities (e.g. Bourrier et al. 2022). The one ESPRESSO observation obtained during transit does not seem compatible with an aligned orbit (Fig. A.4), but this will have to be confirmed with further observations.

TOI-4860 is located precisely at the fully convective boundary (Chabrier & Baraffe 1997), which can influence the star's angular momentum evolution (Irwin et al. 2011). Furthermore, due to the high levels of stellar activity, it can lead to increased stellar wind pressures that can strip away planetary atmospheres, particularly for close-in planets.

The RVs show evidence of an eccentric planet candidate (e = 0.66 ± 0.09) with a period of 427 ± 7 days and a minimum mass of 1.66 ± 0.26 M_J. More data are needed to confirm this second planet, but this raises the possibility that TOI-4860 b ended up in its small-periapsis orbit through planet-planet scattering or Kozai resonance with the outer planet, and then became circularised by tides.

Acknowledgements. We are grateful to the ESO/La Silla staff for their continuous support. We acknowledge funding from the European Research Council under the ERC Grant Agreement no. 337591-ExTrA. This paper includes data collected by the TESS mission. Funding for the TESS mission is provided by the NASA Explorer Program. We acknowledge the use of public TESS data from the pipelines at the TESS Science Office and at the TESS Science Processing Operations Center. Resources supporting this work were provided by the NASA High-End Computing (HEC) program through the NASA Advanced Supercomputing (NAS) Division at Ames Research Center for the production of the SPOC data products. Based on observations obtained at the Canada-France-Hawaii Telescope (CFHT) which is operated from the summit of Maunakea by the National Research Council of Canada, the Institut National des Sciences de l'Univers of the Centre National de la Recherche Scientifique of France, and the University of Hawaii. The observations at the Canada-France-Hawaii Telescope were performed with care and respect from the summit of Maunakea which is a significant cultural and historic site. Based on observations obtained with SPIRou, an international project led by Institut de Recherche en Astrophysique et Planétologie, Toulouse, France. We thank the Swiss National Science Foundation (SNSF) and the Geneva University for their continuous support to our planet search programs. This work has been carried out within the framework of the National Centre of Competence in Research PlanetS supported by the Swiss National Science Foundation under grants 51NF40_182901 and 51NF40_205606. The authors acknowledge the financial support of the SNSF. A.J., R.B., and M.H. acknowledge support from ANID – Millennium Science Initiative – ICN12_009. A.J. acknowledges additional support from FONDECYT project 1210718. R.B. acknowledges support from FONDECYT Project 11200751. E.M. acknowledges funding from FAPEMIG under project number APQ-02493-22 and research productivity grant number 309829/2022-4 awarded by the CNPq, Brazil. X.B., G.H., E.M., A.C., X.D., J.-F.D., T.F., P.F. and C.M. acknowledge funding from the French ANR under contract number ANR18CE310019 (SPlaSH). X.D., X.B., T.F., and A.C. acknowledge funding from the French National Research Agency in the framework of the Investissements d'Avenir program (ANR-15-IDEX-02), through the funding of the "Origin of Life" project of the Grenoble-Alpes University. E.G. acknowledges funding from NASA Award 80NSSC20K0957 (Exoplanets Research Program). This work made use of `tpfplotter` by J. Lillo-Box (publicly available in www.github.com/jlillo/tpfplotter), which also made use of the python packages `astropy`, `lightkurve`, `matplotlib` and `numpy`. This research was carried out in part at the Jet Propulsion Laboratory, California Institute of Technology, under a contract with the National Aeronautics and Space Administration (NASA). D.R. was supported by NASA under award number NNA16BD14C for NASA Academic Mission Services. This work has made use of data from the European Space Agency (ESA) mission *Gaia* (https://www.cosmos.esa.int/gaia), processed by the *Gaia* Data Processing and Analysis Consortium (DPAC, https://www.cosmos.esa.int/web/gaia/dpac/consortium). Funding for the DPAC has been provided by national institutions, in particular, the institutions participating in the *Gaia* Multilateral Agreement. A.C. acknowledges support from CFisUC (UIDB/04564/2020 and UIDP/04564/2020), GRAVITY (PTDC/FIS-AST/7002/2020), and ENGAGE SKA (POCI-01-0145-FEDER-022217), funded by COMPETE 2020 and FCT, Portugal. J.F.D. acknowledges funding from the European Research Council (ERC) under the H2020 research & innovation program (grant agreement #740651 NewWorlds). J.H.C.M. is supported in the form of a work contract funded by Fundação para a Ciência e Tecnologia (FCT) with the reference DL 57/2016/CP1364/CT0007; and also supported from by FCT – Fundação para a Ciência e a Tecnologia through national funds and by FEDER through COMPETE2020 – Programa Operacional Competitividade e Internacionalização by these grants: UIDB/04434/2020; UIDP/04434/2020. J.H.C.M. also acknowledges funding by the European Union (ERC, FIERCE, 101052347). Views and opinions expressed are however those of the author(s) only and do not necessarily reflect those of the European Union or the European Research Council. Neither the European Union nor the granting authority can be held responsible for them. This research has made use of the Spanish Virtual Observatory (https://svo.cab.inta-csic.es) project funded by MCIN/AEI/10.13039/501100011033/ through grant PID2020-112949GB-I00.

The Pan-STARRS1 Surveys (PS1) and the PS1 public science archive have been made possible through contributions by the Institute for Astronomy, the University of Hawaii, the Pan-STARRS Project Office, the Max-Planck Society and its participating institutes, the Max Planck Institute for Astronomy, Heidelberg and the Max Planck Institute for Extraterrestrial Physics, Garching, The Johns Hopkins University, Durham University, the University of Edinburgh, the Queen's University Belfast, the Harvard-Smithsonian Center for Astrophysics, the Las Cumbres Observatory Global Telescope Network Incorporated, the National Central University of Taiwan, the Space Telescope Science Institute, the National Aeronautics and Space Administration under Grant No. NNX08AR22G issued through the Planetary Science Division of the NASA Science Mission Directorate, the National Science Foundation Grant No. AST-1238877, the University of Maryland, Eotvos Lorand University (ELTE), the Los Alamos National Laboratory, and the Gordon and Betty Moore Foundation. This research was carried out in part at the Jet Propulsion Laboratory, California Institute of Technology, under a contract with the National Aeronautics and Space Administration (80NM0018D0004). The Digitized Sky Surveys were produced at the Space Telescope Science Institute under U.S. Government grant NAG W-2166. The images of these surveys are based on photographic data obtained using the Oschin Schmidt Telescope on Palomar Mountain and the UK Schmidt Telescope.

References

Agol, E., Steffen, J., Sari, R., & Clarkson, W. 2005, MNRAS, 359, 567
Akinsanmi, B., Barros, S. C. C., Santos, N. C., et al. 2019, A&A, 621, A117
Allard, F., Homeier, D., & Freytag, B. 2012, Philos. Trans. Roy. Soc. Lond. Ser. A, 370, 2765
Aller, A., Lillo-Box, J., Jones, D., Miranda, L. F., & Barceló Forteza, S. 2020, A&A, 635, A128
Ambikasaran, S., Foreman-Mackey, D., Greengard, L., Hogg, D. W., & O'Neil, M. 2015, IEEE Trans. Pattern Anal. Mach. Intell., 38, 252
Andrews, S. M., Rosenfeld, K. A., Kraus, A. L., & Wilner, D. J. 2013, ApJ, 771, 129
Artigau, É., Astudillo-Defru, N., Delfosse, X., et al. 2014, SPIE Conf. Ser., 9149, 914905
Artigau, É., Cadieux, C., Cook, N. J., et al. 2022, AJ, 164, 84
Astudillo-Defru, N., Delfosse, X., Bonfils, X., et al. 2017, A&A, 600, A13
Bakos, G., Noyes, R. W., Kovács, G., et al. 2004, PASP, 116, 266
Bakos, G. Á., Csubry, Z., Penev, K., et al. 2013, PASP, 125, 154
Bakos, G. Á., Bayliss, D., Bento, J., et al. 2020, AJ, 159, 267
Baranne, A., Queloz, D., Mayor, M., et al. 1996, A&AS, 119, 373
Barros, S. C. C., Akinsanmi, B., Boué, G., et al. 2022, A&A, 657, A52
Bayliss, D., Gillen, E., Eigmüller, P., et al. 2018, MNRAS, 475, 4467
Beleznay, M., & Kunimoto, M. 2022, MNRAS, 516, 75
Bertaux, J. L., Lallement, R., Ferron, S., Boonne, C., & Bodichon, R. 2014, A&A, 564, A46
Bonfils, X., Forveille, T., Delfosse, X., et al. 2005, A&A, 443, L15
Bonfils, X., Almenara, J. M., Jocou, L., et al. 2015, SPIE Conf. Ser., 9605, 96051L
Bouchy, F., Pepe, F., & Queloz, D. 2001, A&A, 374, 733
Bourrier, V., Zapatero Osorio, M. R., Allart, R., et al. 2022, A&A, 663, A160
Bryant, E. M., Bayliss, D., & Van Eylen, V. 2023, MNRAS, 521, 3663
Burn, R., Schlecker, M., Mordasini, C., et al. 2021, A&A, 656, A72
Cañas, C. I., Kanodia, S., Bender, C. F., et al. 2022, AJ, 164, 50
Cadieux, C., Doyon, R., Plotnykov, M., et al. 2022, AJ, 164, 96
Caldwell, D. A., Tenenbaum, P., Twicken, J. D., et al. 2020, RNAAS, 4, 201
Chabrier, G., & Baraffe, I. 1997, A&A, 327, 1039
Chambers, K. C., Magnier, E. A., Metcalfe, N., et al. 2016, arXiv e-prints, [arXiv:1612.05560]
Chandrasekhar, S. 1987, Ellipsoidal figures of equilibrium (New York: Dover)
Ciardi, D. R., Beichman, C. A., Horch, E. P., & Howell, S. B. 2015, ApJ, 805, 16
Cointepas, M., Almenara, J. M., Bonfils, X., et al. 2021, A&A, 650, A145
Cook, N. J., Artigau, É., Doyon, R., et al. 2022, PASP, 134, 114509
Correia, A. C. M. 2014, A&A, 570, A5
Cutri, R. M., Skrutskie, M. F., van Dyk, S., et al. 2003, VizieR Online Data Catalog: II/246
Cutri, R. M., et al. 2013, VizieR Online Data Catalog: II/328
Delfosse, X., Forveille, T., Mayor, M., et al. 1998, , A&A, 338, L67
Díaz, R. F., Almenara, J. M., Santerne, A., et al. 2014, , MNRAS, 441, 983
Donati, J. F., Semel, M., Carter, B. D., Rees, D. E., & Collier Cameron, A. 1997, MNRAS, 291, 658
Donati, J. F., Kouach, D., Moutou, C., et al. 2020, , MNRAS, 498, 5684
Dungee, R., van Saders, J., Gaidos, E., et al. 2022, ApJ, 938, 118
Endl, M., Cochran, W. D., Kürster, M., et al. 2006, ApJ, 649, 436
Espinoza, N. 2018, RNAAS, 2, 209
Espinoza, N., Kossakowski, D., & Brahm, R. 2019, MNRAS, 490, 2262
Fischer, D. A., & Valenti, J. 2005, ApJ, 622, 1102
Foreman-Mackey, D., Agol, E., Ambikasaran, S., & Angus, R. 2017, AJ, 154, 220
Fulton, B. J., Petigura, E. A., Blunt, S., & Sinukoff, E. 2018, PASP, 130, 044504
Gaia Collaboration (Prusti, T., et al.) 2016, A&A, 595, A1
Gaia Collaboration. 2022, VizieR Online Data Catalog: I/357
Gaia Collaboration (Brown, A. G. A., et al.) 2018, A&A, 616, A1
Gaia Collaboration (Vallenari, A., et al.) 2023, A&A, 674, A1
Gaidos, E. 2017, MNRAS, 470, L1
Gaidos, E., Anderson, D. R., Lépine, S., et al. 2014, MNRAS, 437, 3133
Gaidos, E., Claytor, Z., Dungee, R., Ali, A., & Feiden, G. A. 2023, MNRAS, 520, 5283
Gan, T., Soubkiou, A., Wang, S. X., et al. 2022, MNRAS, 514, 4120
Gan, T., Wang, S. X., Wang, S., et al. 2023, AJ, 165, 17
Gregory, P. C. 2005, ApJ, 631, 1198
Guerrero, N. M., Seager, S., Huang, C. X., et al. 2021, ApJS, 254, 39
Hartman, J. D., Bayliss, D., Brahm, R., et al. 2015, AJ, 149, 166
Hobson, M. J., Bouchy, F., Cook, N. J., et al. 2021, A&A, 648, A48
Hobson, M. J., Jordán, A., Bryant, E. M., et al. 2023, ApJ, 946, L4
Holman, M. J., & Murray, N. W. 2005, Science, 307, 1288
Huang, C. X., Vanderburg, A., Pál, A., et al. 2020a, RNAAS, 4, 204
Huang, C. X., Vanderburg, A., Pál, A., et al. 2020b, RNAAS, 4, 206
Ilic, N., Poppenhaeger, K., & Hosseini, S. M. 2022, MNRAS, 513, 4380
Irwin, J. B. 1952, ApJ, 116, 211
Irwin, J., Berta, Z. K., Burke, C. J., et al. 2011, ApJ, 727, 56
Jenkins, J. M. 2002, ApJ, 575, 493
Jenkins, J. M., Chandrasekaran, H., McCauliff, S. D., et al. 2010, SPIE Conf. Ser., 7740, 77400D
Jenkins, J. M., Twicken, J. D., McCauliff, S., et al. 2016, SPIE Conf. Ser., 9913, 99133E
Jenkins, J. M., Tenenbaum, P., Seader, S., et al. 2020, Kepler Data Processing Handbook: Transiting Planet Search, Kepler Data Processing Handbook (KSCI-19081-003)
Johnson, J. A., Butler, R. P., Marcy, G. W., et al. 2007, ApJ, 670, 833
Jordán, A., Hartman, J. D., Bayliss, D., et al. 2022, AJ, 163, 125
Kagetani, T., Narita, N., Kimura, T., et al. 2023, PASJ, 75, 713
Kanodia, S., & Wright, J. 2018, RNAAS, 2, 4
Kanodia, S., Libby-Roberts, J., Cañas, C. I., et al. 2022, AJ, 164, 81
Kanodia, S., Mahadevan, S., Libby-Roberts, J., et al. 2023, AJ, 165, 120
Kass, R. E., & Raftery, A. E. 1995, J. Am. Stat. Assoc., 90, 773
Kempton, E. M. R., Bean, J. L., Louie, D. R., et al. 2018, PASP, 130, 114401
Kiefer, F., Hébrard, G., Martioli, E., et al. 2023, A&A, 670, A136
Kiman, R., Faherty, J. K., Cruz, K. L., et al. 2021, AJ, 161, 277
Kipping, D. M. 2010, MNRAS, 408, 1758
Kipping, D. M. 2013, MNRAS, 435, 2152
Koornneef, J., Bohlin, R., Buser, R., Horne, K., & Turnshek, D. 1986, Highlights Astron., 7, 833
Kreidberg, L. 2015, PASP, 127, 1161
Kunimoto, M., Huang, C., Tey, E., et al. 2021, RNAAS, 5, 234
Kunimoto, M., Daylan, T., Guerrero, N., et al. 2022, ApJS, 259, 33
Lasker, B. M., Doggett, J., McLean, B., et al. 1996, in Astronomical Data Analysis Software and Systems V, eds. G. H. Jacoby, & J. Barnes, Astronomical Society of the Pacific Conference Series, 101, 88
Laughlin, G., Bodenheimer, P., & Adams, F. C. 2004, ApJ, 612, L73
Lecavelier Des Etangs, A. 2007, A&A, 461, 1185
Li, J., Tenenbaum, P., Twicken, J. D., et al. 2019, PASP, 131, 024506
Lindegren, L., Klioner, S. A., Hernández, J., et al. 2021, A&A, 649, A2
Luger, R., Agol, E., Foreman-Mackey, D., et al. 2019, AJ, 157, 64
Maciejewski, G., Fernández, M., Aceituno, F., et al. 2018, Acta Astron., 68, 371
Mann, A. W., Feiden, G. A., Gaidos, E., Boyajian, T., & von Braun, K. 2015, ApJ, 804, 64
Mann, A. W., Dupuy, T., Kraus, A. L., et al. 2019, ApJ, 871, 63
Marcy, G. W., Butler, R. P., Vogt, S. S., Fischer, D., & Lissauer, J. J. 1998, ApJ, 505, L147
Martioli, E., Hébrard, G., Moutou, C., et al. 2020, A&A, 641, L1
Martioli, E., Hébrard, G., Fouqué, P., et al. 2022, A&A, 660, A86
Mathis, S. 2015, A&A, 580, L3
Mayor, M., & Queloz, D. 1995, Nature, 378, 355
McLaughlin, D. B. 1924, ApJ, 60, 22
Minkowski, R. L., & Abell, G. O. 1963, in Basic Astronomical Data: Stars and Stellar Systems, ed. K. A. Strand, 481
Mugrauer, M., & Michel, K.-U. 2020, Astron. Nachr., 341, 996
Mugrauer, M., & Michel, K.-U. 2021, Astron. Nachr., 342, 840
Newton, E. R., Irwin, J., Charbonneau, D., et al. 2017, ApJ, 834, 85
Parviainen, H., Palle, E., Zapatero-Osorio, M. R., et al. 2021, A&A, 645, A16
Patra, K. C., Winn, J. N., Holman, M. J., et al. 2017, AJ, 154, 4
Pecaut, M. J., & Mamajek, E. E. 2013, ApJS, 208, 9
Pepe, F., Mayor, M., Galland, F., et al. 2002, A&A, 388, 632

Pepe, F., Cristiani, S., Rebolo, R., et al. 2021, A&A, 645, A96
Pollacco, D. L., Skillen, I., Collier Cameron, A., et al. 2006, PASP, 118, 1407
Popinchalk, M., Faherty, J. K., Kiman, R., et al. 2021, ApJ, 916, 77
Ragozzine, D., & Wolf, A. S. 2009, ApJ, 698, 1778
Rein, H., & Liu, S. F. 2012, A&A, 537, A128
Ricker, G. R., Winn, J. N., Vanderspek, R., et al. 2015, J. Astron. Telescopes Instrum. Syst., 1, 014003
Riello, M., De Angeli, F., Evans, D. W., et al. 2021, A&A, 649, A3
Rodrigo, C., & Solano, E. 2020, in XIV.0 Scientific Meeting (virtual) of the Spanish Astronomical Society, 182
Rodrigo, C., Solano, E., & Bayo, A. 2012, SVO Filter Profile Service Version 1.0, IVOA Working Draft 15 October 2012
Rossiter, R. A. 1924, ApJ, 60, 15
Skrutskie, M. F., Cutri, R. M., Stiening, R., et al. 2006, AJ, 131, 1163
Smith, J. C., Stumpe, M. C., Van Cleve, J. E., et al. 2012, PASP, 124, 1000
Speagle, J. S. 2020, MNRAS, 493, 3132
Stassun, K. G., Oelkers, R. J., Paegert, M., et al. 2019, AJ, 158, 138
Stumpe, M. C., Smith, J. C., Van Cleve, J. E., et al. 2012, PASP, 124, 985
Stumpe, M. C., Smith, J. C., Catanzarite, J. H., et al. 2014, PASP, 126, 100
Tayar, J., Claytor, Z. R., Huber, D., & van Saders, J. 2022, ApJ, 927, 31
Triaud, A. H. M. J., Dransfield, G., Kagetani, T., et al. 2023, MNRAS, 525, L98
Twicken, J. D., Catanzarite, J. H., Clarke, B. D., et al. 2018, PASP, 130, 064502
Wang, S. X., Latouf, N., Plavchan, P., et al. 2022, AJ, 164, 211
Wizinowich, P., Acton, D. S., Shelton, C., et al. 2000, PASP, 112, 315
Wright, J. T., & Eastman, J. D. 2014, PASP, 126, 838
Wright, E. L., Eisenhardt, P. R. M., Mainzer, A. K., et al. 2010, AJ, 140, 1868
Yee, S. W., Petigura, E. A., & von Braun, K. 2017, ApJ, 836, 77
Zechmeister, M., & Kürster, M. 2009, A&A, 496, 577
Ziegler, C., Tokovinin, A., Briceño, C., et al. 2020, AJ, 159, 19

[1] Univ. Grenoble Alpes, CNRS, IPAG, 38000 Grenoble, France
e-mail: jose-manuel.almenara-villa@univ-grenoble-alpes.fr
[2] Observatoire de Genève, Département d'Astronomie, Université de Genève, Chemin Pegasi 51b, 1290 Versoix, Switzerland
[3] Mullard Space Science Laboratory, University College London, Holmbury St Mary, Dorking, Surrey RH5 6NT, UK
[4] Department of Physics, University of Warwick, Coventry, UK
[5] Facultad de Ingeniería y Ciencias, Universidad Adolfo Ibáñez, Av. Diagonal las Torres 2640, Peñalolén, Santiago, Chile
[6] Millennium Institute for Astrophysics (MAS), Santiago, Chile
[7] Data Observatory Foundation, Santiago, Chile
[8] Institut d'astrophysique de Paris, UMR7095 CNRS, Université Pierre & Marie Curie, 98bis boulevard Arago, 75014 Paris, France
[9] Observatoire de Haute-Provence, CNRS, Université d'Aix-Marseille, 04870 Saint-Michel-l'Observatoire, France
[10] Laboratório Nacional de Astrofísica, Rua Estados Unidos 154, 37504-364, Itajubá, MG, Brazil
[11] CFisUC, Departamento de Física, Universidade de Coimbra, 3004-516 Coimbra, Portugal
[12] IMCCE, UMR8028 CNRS, Observatoire de Paris, PSL Université, Sorbonne Univ., 77 av. Denfert-Rochereau, 75014 Paris, France
[13] Departamento de Matemática y Física Aplicadas, Universidad Católica de la Santísima Concepción, Alonso de Rivera 2850, Concepción, Chile
[14] Université de Montréal, Département de Physique & Institut Trottier de Recherche sur les Exoplanètes, Montréal, QC H3C 3J7, Canada
[15] Canada-France-Hawaii Telescope (CFHT) Corporation, CNRS UAR2208, 65-1238 Mamalahoa Hwy, Kamuela, HI 96743, USA
[16] Department of Astrophysical Sciences, Princeton University, NJ 08544, USA
[17] Instituto de Astrofísica e Ciências do Espaço, Universidade do Porto, CAUP, Rua das Estrelas, 4150-762 Porto, Portugal
[18] Departamento de Fisica e Astronomia, Faculdade de Ciencias, Universidade do Porto, Rua Campo Alegre, 4169-007 Porto, Portugal
[19] Center for Astrophysics | Harvard & Smithsonian, 60 Garden Street, Cambridge, MA 02138, USA
[20] NASA Exoplanet Science Institute – Caltech/IPAC, 1200 E. California Blvd, Pasadena, CA 91125, USA
[21] Department of Physics & Astronomy, McMaster University, 1280 Main St W, Hamilton, ON L8S 4L8, Canada
[22] Department of Physics, McGill University, 3600 rue University, Montréal, Québec H3A 2T8, Canada
[23] Department of Earth and Planetary Sciences, McGill University, 3450 rue University, Montréal, Québec H3A 0E8, Canada
[24] Univ. Federal do Rio G. do Norte, UFRN, Dep. de Física, CP 1641, 59072-970, Natal, RN, Brazil
[25] Université de Toulouse, CNRS, IRAP, 14 avenue Belin, 31400 Toulouse, France
[26] Dept. of Earth Sciences, University of Hawai'i at Mänoa, Honolulu, HI 96822, USA
[27] Jet Propulsion Laboratory, California Institute of Technology, 4800 Oak Grove Drive, Pasadena, CA 91109, USA
[28] Wesleyan University, Middletown, CT 06459, USA
[29] Max Planck Institute for Astronomy, Königstuhl 17, 69117 Heidelberg, Germany
[30] NASA Ames Research Center, Moffett Field, CA 94035, USA
[31] LESIA, Observatoire de Paris, Université PSL, CNRS, Sorbonne Université, Université Paris Cité, 5 place Jules Janssen, 92195 Meudon, France
[32] NASA Goddard Space Flight Center, 8800 Greenbelt Road, Greenbelt, MD 20771, USA
[33] SETI Institute, 189 Bernardo Ave, Suite 200, Mountain View, CA 94043, USA
[34] Physics & Astrophysics Group, Dept. of Physical & Environmental Sciences, University of Toronto Scarborough, 1265 Military Trail, Toronto, Ontario, M1C 1A4, Canada
[35] David A. Dunlap Department of Astronomy & Astrophysics, University of Toronto. 50 St. George Street, Toronto, Ontario M5S 3H4, Canada
[36] Department of Physics, University of Toronto, 60 St George Street, Toronto, Ontario M5S 1A7, Canada
[37] Instituto de Astrofísica de Canarias (IAC), 38200 La Laguna, Tenerife, Spain
[38] Dept. Astrofísica, Universidad de La Laguna (ULL), 38206 La Laguna, Tenerife, Spain
[39] Department of Physics and Astronomy, University of Kansas, 1251 Wescoe Hall Drive, Lawrence, KS 66045, USA
[40] Research Institute for Advanced Computer Science, Universities Space Research Association, Washington, DC 20024, USA
[41] European Southern Observatory, Alonso de Córdova 3107, Vitacura, Región Metropolitana, Chile
[42] Institute of Astronomy and Astrophysics, Academia Sinica, Taipei 10617, Taiwan

Appendix A: Additional figures and tables

Table A.1. Modelling of the SED.

Parameter		Prior	Posterior median and 68.3% CI
Effective temperature, $T_{\rm eff}$	[K]	N(3191, 70)	3260±50
Surface gravity, $\log g$	[cgs]	U(-0.5, 6.0)	$5.4^{+0.5}_{-0.7}$
Metallicity, [Fe/H]	[dex]	N(0.27, 0.12)	0.25 ± 0.12
Distance	[pc]	N(80.42, 0.22)	80.42 ± 0.22
$E_{(\rm B-V)}$	[mag]	U(0, 3)	$0.039^{+0.05}_{-0.029}$
Jitter *Gaia*	[mag]	U(0, 1)	$0.16^{+0.21}_{-0.08}$
Jitter 2MASS	[mag]	U(0, 1)	$0.027^{+0.06}_{-0.020}$
Jitter WISE	[mag]	U(0, 1)	$0.09^{+0.19}_{-0.07}$
Radius, $R_\star$	[$R_\odot$]	U(0, 100)	0.371±0.010
Luminosity	[$L_\odot$]		0.0139± 0.0006

Notes. $N(\mu,\sigma)$: Normal distribution prior with mean μ, and standard deviation σ. U(l,u): Uniform distribution prior in the range [l, u].

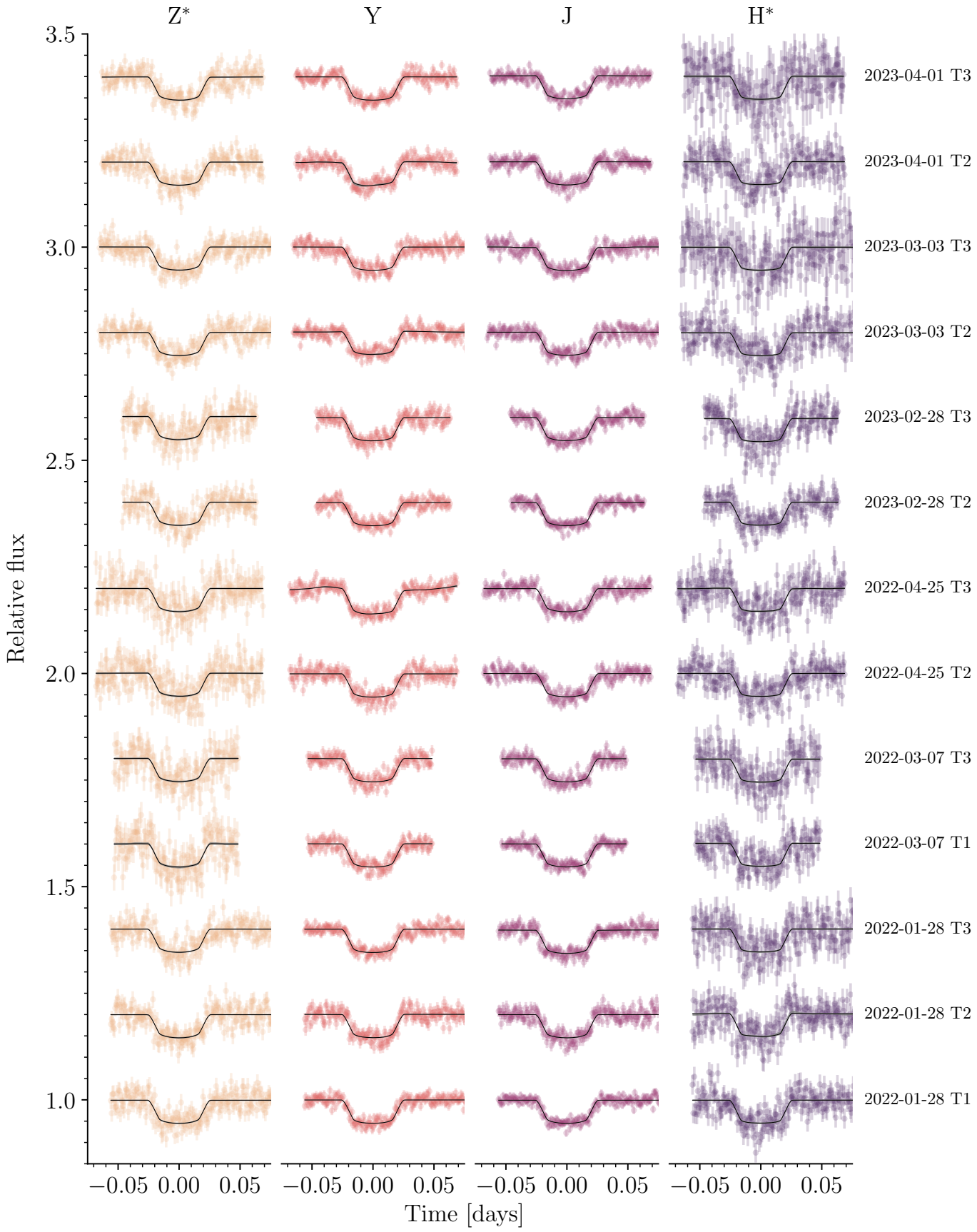

Fig. A.1. ExTrA transit photometry observations of TOI-4860 b in the Z*, Y, J, and H* bands (error bars). Each line corresponds to a night (with format YYYY-MM-DD) and ExTrA telescope (labelled T1, T2, and T3) observation, which are offset vertically for clarity. For each transit, the median model (black line) and 68% CI (grey band, barely visible) computed from 1000 random posterior samples are shown.

Table A.2. RV measurements.

Time [BJD_{TDB}]	RV ($m\,s^{-1}$)	$\pm1\,\sigma$ ($m\,s^{-1}$)	Exposure time [s]	Instrument	Time [BJD_{TDB}]	RV ($m\,s^{-1}$)	$\pm1\,\sigma$ ($m\,s^{-1}$)	Exposure time [s]	Instrument
2459651.014632[a]	20672.79	35.56	184	SPIRou	2459737.789964	20635.10	16.42	602	SPIRou
2459651.017018[a]	20728.73	38.07	184	SPIRou	2459737.797252	20656.47	15.27	602	SPIRou
2459651.019405[a]	20727.25	38.52	184	SPIRou	2459741.833491	20510.06	14.71	602	SPIRou
2459651.021792[a]	20783.75	41.44	184	SPIRou	2459741.840779	20569.59	14.97	602	SPIRou
2459652.016441	20635.91	31.35	184	SPIRou	2459741.848004	20518.22	15.84	602	SPIRou
2459652.018828	20655.03	32.13	184	SPIRou	2459741.855228	20521.80	16.34	602	SPIRou
2459652.021215	20594.47	32.59	184	SPIRou	2459974.822807	20519.66	1.18	2400	ESPRESSO
2459652.023602	20609.83	33.11	184	SPIRou	2459975.790100[b,c]	20592.20	1.62	2400	ESPRESSO
2459682.962344	20667.94	15.51	602	SPIRou	2459990.710841	20676.61	1.40	2400	ESPRESSO
2459682.969568	20689.38	15.49	602	SPIRou	2459994.713548	20542.96	1.73	2400	ESPRESSO
2459682.976857	20672.99	15.11	602	SPIRou	2459995.728387	20524.94	1.39	2400	ESPRESSO
2459682.984081	20675.06	15.54	602	SPIRou	2459996.704515	20681.57	1.13	2400	ESPRESSO
2459683.975195	20438.47	15.71	602	SPIRou	2459998.681241	20556.29	1.78	2400	ESPRESSO
2459683.982484	20553.25	15.54	602	SPIRou	2460034.973275	20747.20	16.20	602	SPIRou
2459683.989773	20480.31	16.34	602	SPIRou	2460034.980499	20691.66	15.74	602	SPIRou
2459683.996998	20506.34	17.13	602	SPIRou	2460034.987723	20728.46	16.72	602	SPIRou
2459688.978921	20589.02	14.55	602	SPIRou	2460034.994948	20750.87	16.75	602	SPIRou
2459688.986145	20617.96	15.26	602	SPIRou	2460064.881853	20636.17	20.74	602	SPIRou
2459688.993370	20667.28	15.46	602	SPIRou	2460064.889078	20628.63	38.55	602	SPIRou
2459689.000595	20677.68	15.52	602	SPIRou	2460064.896367[a,c]	20688.17	50.19	602	SPIRou
2459689.971959	20475.41	15.64	602	SPIRou	2460064.903591[a,c]	20764.02	60.23	602	SPIRou
2459689.979248	20550.51	15.97	602	SPIRou	2460069.886522	20717.37	13.70	602	SPIRou
2459689.986473	20536.16	16.77	602	SPIRou	2460069.893810	20705.09	14.03	602	SPIRou
2459689.993697	20539.39	16.53	602	SPIRou	2460069.901034	20715.34	14.51	602	SPIRou
2459690.966227	20586.54	15.28	602	SPIRou	2460069.908259	20698.83	14.95	602	SPIRou
2459690.973517	20577.52	15.71	602	SPIRou	2460075.860806	20730.24	14.42	602	SPIRou
2459690.980745	20631.14	16.52	602	SPIRou	2460075.868095	20768.85	13.83	602	SPIRou
2459690.988031	20561.25	16.73	602	SPIRou	2460075.875383	20695.31	13.50	602	SPIRou
2459711.923333	20627.61	16.30	602	SPIRou	2460075.882608	20707.40	13.94	602	SPIRou
2459711.930622	20583.55	17.47	602	SPIRou	2460076.879995	20502.99	14.82	602	SPIRou
2459711.937910	20631.63	17.86	602	SPIRou	2460076.887283	20542.48	16.61	602	SPIRou
2459711.945134	20662.24	17.92	602	SPIRou	2460076.894508	20505.84	15.54	602	SPIRou
2459712.898086	20302.36	15.85	602	SPIRou	2460076.901732	20556.08	15.46	602	SPIRou
2459712.905375	20438.74	18.02	602	SPIRou	2460096.784419	20513.62	17.24	602	SPIRou
2459712.912599	20394.84	16.58	602	SPIRou	2460096.791645	20606.75	16.41	602	SPIRou
2459712.919823	20455.80	17.72	602	SPIRou	2460096.798874	20581.53	17.00	602	SPIRou
2459714.871905	20549.95	16.01	602	SPIRou	2460096.806090[a,c]	21324.07	73.70	602	SPIRou
2459714.879195	20642.84	16.56	602	SPIRou	2460098.813093	20731.23	25.57	602	SPIRou
2459714.886419	20591.96	17.63	602	SPIRou	2460098.820377	20615.90	21.33	602	SPIRou
2459714.893708	20547.20	18.88	602	SPIRou	2460098.827671	20714.14	22.61	602	SPIRou
2459715.894581	20418.06	15.11	602	SPIRou	2460098.834895	20749.88	23.10	602	SPIRou
2459715.901869	20457.61	15.26	602	SPIRou	2460102.846326	20522.33	13.25	602	SPIRou
2459715.909158	20434.95	15.93	602	SPIRou	2460102.853615	20553.68	13.26	602	SPIRou
2459715.916382	20499.60	17.42	602	SPIRou	2460102.860903	20551.93	13.50	602	SPIRou
2459716.903709[b]	20550.12	13.69	602	SPIRou	2460102.868127	20566.81	13.76	602	SPIRou
2459716.910997[b]	20534.58	14.51	602	SPIRou	2460124.740016	20611.59	16.83	602	SPIRou
2459716.918222[b]	20486.82	14.86	602	SPIRou	2460124.747305	20601.19	16.32	602	SPIRou
2459716.925446[b]	20534.29	15.74	602	SPIRou	2460124.754594	20615.81	16.28	602	SPIRou
2459717.904838	20430.67	21.65	602	SPIRou	2460124.761820	20651.56	16.51	602	SPIRou
2459717.912126	20535.44	25.12	602	SPIRou	2460128.751561	20552.08	18.63	602	SPIRou
2459717.919415	20558.42	24.88	602	SPIRou	2460128.758785	20557.96	17.93	602	SPIRou
2459717.926639	20623.72	27.34	602	SPIRou	2460128.766009	20520.20	18.43	602	SPIRou
2459719.919542	20453.45	16.00	602	SPIRou	2460128.773233	20519.43	21.04	602	SPIRou
2459719.926830	20539.12	17.01	602	SPIRou	2460129.750056	20450.99	24.34	602	SPIRou
2459719.934054[b]	20542.62	27.27	602	SPIRou	2460130.751754	20668.27	13.81	602	SPIRou
2459719.941278[b]	20477.03	23.83	602	SPIRou	2460130.759042	20649.19	13.81	602	SPIRou
2459737.775387	20649.42	15.23	602	SPIRou	2460130.766331	20659.68	14.01	602	SPIRou
2459737.782675	20682.05	15.45	602	SPIRou	2460130.773555	20691.74	14.74	602	SPIRou

Notes. [a]Flagged by the telluric correction algorithm.[b]Observation during transit.[c]Not used in the analysis.

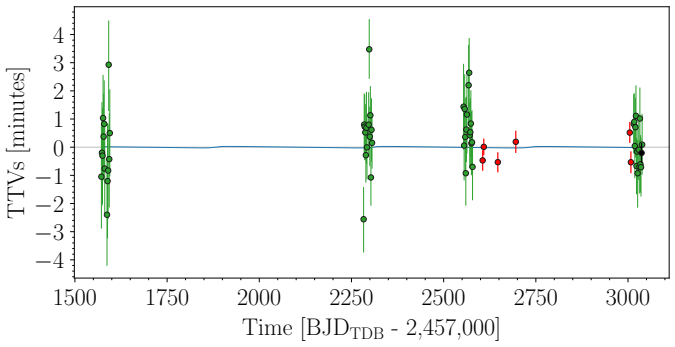

Fig. A.2. TTVs of TOI-4860 b from TESS (green error bars), ExTrA (red error bars), and a transit observed simultaneously by TESS and ExTrA (black error bar). The blue curve is the expected TTVs due to the presence of the planet c candidate.

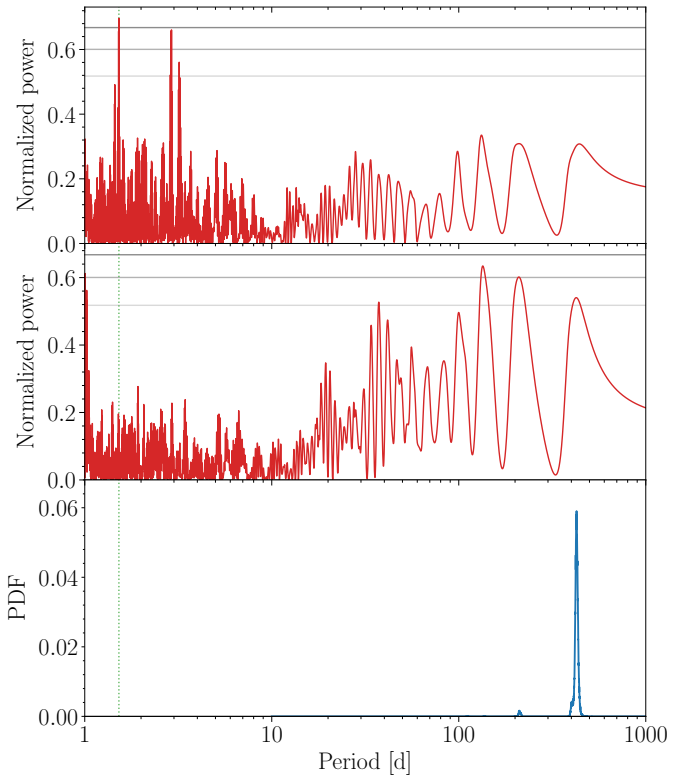

Fig. A.3. Periodogram of the SPIRou data. *Top panel*: generalised Lomb–Scargle (GLS) periodogram (Zechmeister & Kürster 2009) of the nightly averaged SPIRou velocities for TOI-4860 (red line). The horizontal lines represents 10, 1, and 0.1% false-alarm levels, from bottom to top. The vertical dotted green line marks the period of the transiting planet. *Middle panel*: idem after subtracting the Keplerian orbit of planet b. Given that the planet c candidate has a significant eccentricity, the power of the GLS periodogram is partially transferred to the harmonics of the orbital period, which leads to a reduced peak amplitude. *Bottom panel*: marginal posterior distribution of the period of a second planet search with SPIRou and ESPRESSO (Sect. 4.3).

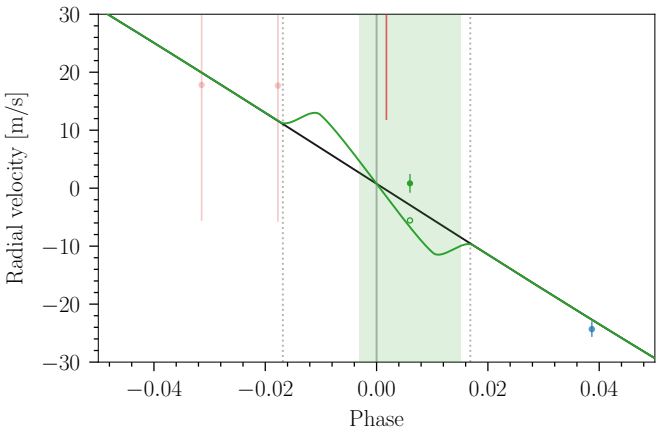

Fig. A.4. Same as the upper panel of Fig. 8 but including the ESPRESSO observation during transit (green error bar), with its phase coverage highlighted in green. The transit centre is marked with a vertical solid grey line, and the ingress and egress are marked with dotted vertical grey lines. The green line is a model for the RVs that includes the Rossiter–McLaughlin effect for an aligned system (computed with the `starry` code; Luger et al. 2019), and the green open circle is the integration of this model for the ESPRESSO observation during transit.